Atmos. Chem. Phys. Discuss., https://doi.org/10.5194/acp-2017-1216
Manuscript under review for journal Atmos. Chem. Phys.
Discussion started: 31 January 2018

Ice cloud microphysical trends observed by the Atmospheric Infrared Sounder

Brian H. Kahn[1], Hanii Takahashi[1,2], Graeme L. Stephens[1], Qing Yue[1], Julien Delanoë[3], Gerald Manipon[1], Evan M. Manning[1], and Andrew J. Heymsfield[4]

[1]Jet Propulsion Laboratory, California Institute of Technology, Pasadena, CA, 91109, USA
[2]Joint Institute for Regional Earth System Science and Engineering, University of California – Los Angeles, Los Angeles, CA, 90095, USA
[3]LATMOS/IPSL, UVSQ-CNRS-UPMC, 11 Boulevard D'Alembert, 78280 Guyancourt, France
[4]National Center for Atmospheric Research, Boulder, CO, 80301, USA

Correspondence to: Brian H. Kahn (brian.h.kahn@jpl.nasa.gov)

Abstract. We use the AIRS version 6 ice cloud property and thermodynamic phase retrievals to quantify variability and 14-year trends in ice cloud frequency, ice cloud top temperature (T_{ci}), ice optical thickness (τ_i) and ice effective radius (r_{ei}). The trends in ice cloud properties are shown to be independent of trends in information content and χ^2. Statistically significant decreases in ice frequency, τ_i, and ice water path (IWP) are found in the SH and NH extratropics, but trends are much smaller and statistically insignificant in the tropics. However, statistically significant increases in r_{ei} are found in all three latitude bands. Perturbation experiments consistent with estimates of AIRS radiometric stability fall significantly short of explaining the observed trends in ice properties, averaging kernels, and χ^2 trends. Values of r_{ei} are larger at the tops of opaque clouds and exhibit strong dependence on surface wind speed, column water vapour (CWV) and surface temperature (T_{sfc}) with changes up to 10–12 μm. Transparent clouds exhibit a much smaller change in r_{ei} for CWV, while none is observed for T_{sfc}. Comparisons between DARDAR and AIRS suggest that r_{ei} is smallest for single-layer cirrus, larger for cirrus above weak convection, and largest for cirrus above strong convection at the same cloud top temperature. This behaviour is consistent with enhanced particle growth from radiative cooling above convection or large particle lofting from strong convection.

1 Introduction

While our understanding of ice cloud microphysics has greatly advanced from targeted in situ campaigns during the past several decades (Baumgardner et al., 2017), global distributions obtained from satellite observing systems remain highly uncertain (e.g., Stubenrauch et al., 2013). Climate GCM simulations of the radiative response of high clouds have a large inter-model spread (e.g., Zelinka et al., 2013). Uncertainty in the ice hydrometeor fall speed is cited as a leading contributor despite dozens of modelling parameters contributing to this spread (e.g., Sanderson et al., 2008). The ice particle size distribution (PSD) is closely correlated to the magnitude of fall speed (Heymsfield et al., 2013; Mitchell et al., 2008). The PSD is frequently summarized as an ice effective radius (r_{ei}) (McFarquhar and Heymsfield, 1998) in most publicly available satellite remote sensing data sets.

Global decadal-scale satellite-based estimates of r_{ei} are available from two algorithm versions of the Moderate Resolution Imaging Spectroradiometer (MODIS) (Platnick et al., 2017; Minnis et al., 2011) and the Atmospheric Infrared Sounder (AIRS) (Kahn et al., 2014). Another estimate of r_{ei} is derived from a combination of the Cloud-Aerosol Lidar with Orthogonal Polarization (CALIOP) and the Imaging Infrared Radiometer (IIR) instruments (Garnier et al., 2013) on the Cloud-Aerosol Lidar and Infrared Pathfinder Satellite Observation (CALIPSO) satellite (Winker et al., 2010). Additional active-passive algorithms are also available. Deng et al. (2013) describe comparisons of r_{ei} between the CloudSat level-2C ice cloud property product (2C-ICE), radar-lidar profiles of r_{ei} (DARDAR; Delanoë and Hogan, 2010), and the CloudSat level-2B radar-visible optical depth cloud water content product (2B-CWC-RVOD).

Satellite retrievals of r_{ei} have known sources of uncertainty that are traced to the use of 1-D radiative transfer theory (e.g., Fauchez et al., 2015), errors that arise from a lack of precision, accuracy, or incomplete sampling in the atmospheric and surface state (e.g., Kahn et al., 2015), variability in mixtures of ice crystal habits and PSDs within a single satellite pixel (e.g., Kahn et al. 2008; Posselt et al., 2008), systematic uncertainties and approximations taken in the forward model (e.g., Wang et al., 2016; Irion et al., 2017), and instrument calibration drift (e.g., Pagano et al., 2012; Yue et al., 2017a; Manning and Aumann, 2017). The vertical heterogeneity of ice water content (IWC) and r_{ei} are known to cause differences in r_{ei} derived from shortwave/near-infrared (SWIR) and mid-infrared (MIR) bands for identical clouds and observing geometry (Zhang et al., 2010). Kahn et al. (2015) compared pixel-scale retrievals between MODIS Collection 6 (C6; Platnick et al., 2017) and AIRS Version 6 (V6; Kahn et al., 2014) and confirmed, for a small subset of homogeneous clouds, that r_{ei} is typically 5–10 μm larger when derived from MODIS SWIR bands compared to AIRS MIR bands.

Secular trends in water path, cloud amount, and cloud height (e.g., Wylie et al., 2005; Dim et al., 2011; Bender et al., 2012; Marvel et al., 2015; Norris et al., 2016; Manaster et al., 2017) suggest that climate change signals may be observable within the satellite era. There is a notable absence of published studies regarding trends in ice microphysics. Sherwood (2002) inferred regional decreases of r_{ei} by ~0.5 μm per decade using offline calculations of Advanced Very High Resolution Radiometer (AVHRR) radiances and argued for the importance of aerosols on cloud microphysics. Chen et al. (2016) describe experiments with the Nonhydrostatic ICosahedral Atmospheric Model (NICAM) that suggest an increase of r_{ei} in a warming climate that may be related to a weaker tropical circulation, and therefore implies changes in the dominant pathways of ice nucleation, growth, and precipitation processes. The rapid intensification of Earth's hydrological cycle is consistent with increased convective aggregation (Mauritsen and Stevens, 2015), the narrowing and intensification of the ITCZ (Su et al., 2017), and a lower end estimate of climate sensitivity; the high cloud response is key to reconcile a strong hydrological response and lower end climate sensitivity (e.g., Lindzen et al., 2001; Mauritsen and Stevens, 2015). The areal extent of cloud anvils are correlated to upper tropospheric lapse rate (Bony et al., 2016) and additionally ice hydrometeor fall speed, with larger (smaller) anvils for smaller (larger) r_{ei} (Satoh and Matsuda, 2009). The radiometrically stable AIRS instrument (Pagano et al., 2012) may provide constraints on ice cloud microphysical properties that are highly desired (Kärcher, 2017).

While not the focus of this investigation, aerosols modulate ice clouds through numerous indirect and direct pathways (Liu et al., 2007; Gettelman et al., 2010; Kärcher, 2017). Variable magnitudes of r_{ei} at convective tops result from variations in cloud condensation nuclei (CCN) or ice nuclei (IN); these responses are highly nonlinear because of complex liquid and ice phase microphysical processes as a function of updraft velocity, concentration and composition of CCN and IN (Phillips et al., 2007; Van Weverberg et al., 2013). Morrison and Grabowski (2011) used a 2-D cloud resolving model (CRM) to show that convection may subtly weaken yet cloud top height and anvil IWC may increase in polluted compared to clean conditions, resulting in a reduction of r_{ei} by up to a factor of two. Simultaneous observations of r_{ei} from MODIS and IWC from the Microwave Limb Sounder (MLS) suggest that more intense convection (defined by positive anomalies of IWC) increases r_{ei} while polluted air (defined by positive anomalies of aerosol τ) decreases r_{ei} (Jiang et al., 2011). Whether convection is dynamically invigorated by increased aerosol concentrations, however, is highly debatable (Rosenfeld et al., 2008; Fan et al., 2013; Grabowski, 2015). Improving our understanding of satellite-based ice cloud microphysics will lay the groundwork for future observational constraints of aerosol-ice microphysics interactions.

Stanford et al. (2017) show that the covariability of cloud temperature, vertical velocity, and r_{ei} observations within tropical mesoscale convective systems (MCSs) reveal very complex behaviour taken during the High Altitude Ice Crystals-High Ice Water Content (HAIC-HIWC) field campaign near Australia. HAIC-HIWC observations and simulations with the Weather Research and Forecasting (WRF) model using multiple microphysical parameterizations are compared. The observations show that larger (smaller) r_{ei} are found in weaker (stronger) updrafts of MCSs, while the reverse is generally true for IWC; however the opposite behaviour was found for observations taken within a tropical cyclone (Leroy et al., 2017). The covariability of r_{ei} with cloud temperature and vertical velocity among the WRF experiments strongly disagree in sign and magnitude compared to HAIC-HIWC observations.

The aforementioned observational, theoretical, and numerical modelling studies motivate the development of additional constraints on r_{ei} and its covariability with other ice cloud, thermodynamic, and dynamic fields. This investigation is a first attempt to quantify secular changes in r_{ei} from AIRS over its decade and a half observational record with well-characterized radiometric stability (Pagano et al., 2012). We attempt to identify potential algorithmic, information content, calibration, and sampling characteristics that induce nonphysical trends. Collocated AIRS and AMSR data are used to glean insight among the connections between r_{ei} and tropical convection/precipitation processes. Lastly, DARDAR data is used to investigate increases in r_{ei} that occur near the tops of deep convection.

2 Data

2.1 Atmospheric Infrared Sounder (AIRS)

The AIRS V6 cloud properties are used from 01 September 2002 until 31 August 2016 (Kahn et al., 2014; K14 hereafter). As this investigation addresses ice microphysics, we focus on the 26.5% of AIRS pixels containing ice thermodynamic phase, and the ice cloud top temperature (T_{ci}), ice optical thickness (τ_i) and r_{ei} parameters (K14). The retrieval of cloud thermodynamic phase is described in K14 and is validated against CALIOP phase estimates in Jin and Nasiri (2014). A set of four brightness temperature (T_b) thresholds and T_b differences (ΔT_b) in the 8–12 μm atmospheric window region identify ice phase by leveraging the spectral dependence of the refractive index of ice, and is identified in excess of 90% of the time using CALIOP as truth. Ice clouds of convective origin typically have larger τ_i (Krämer et al., 2016) and trigger more of the ice phase tests, while tenuous ice clouds have smaller τ_i and trigger fewer phase tests.

For each AIRS footprint identified as containing ice, the three-parameter optimal estimation (OE) ice cloud property retrieval is performed (K14) and minimizes the following cost function:

$$C = \|\boldsymbol{y} - \boldsymbol{F}(\boldsymbol{x}, \boldsymbol{b})\|^2_{\boldsymbol{S}_{\boldsymbol{\varepsilon}}^{-1}} + \|\boldsymbol{x} - \boldsymbol{x}_{\boldsymbol{a}}\|^2_{\boldsymbol{S}_{\boldsymbol{a}}^{-1}}, \quad (1)$$

where ***F(x)*** is the radiance vector that is forward modelled, $\boldsymbol{x}$ is the state vector of retrieved parameters, $\boldsymbol{b}$ is the vector containing fixed state parameters, $\boldsymbol{y}$ is the vector of AIRS radiances (K14), $\boldsymbol{x}_{\boldsymbol{a}}$ is the prior guess of $\boldsymbol{x}$, $\boldsymbol{S}_{\boldsymbol{a}}^{-1}$ is the inverse of the a priori covariance, and $\boldsymbol{S}_{\boldsymbol{\varepsilon}}^{-1}$ is the inverse of the noise covariance of AIRS radiances. The retrieval state vector $\boldsymbol{x}$ is restricted to τ_i (ice_cld_opt_dpth in L2 Support file; defined at 0.55 μm), r_{ei} (ice_cld_eff_diam in L2 Support file; D_e is converted to r_{ei} henceforth), and T_{ci} (ice_cld_temp_eff in L2 Support file). The bulk ice scattering models, and the definition of ice D_e, follows from Baum et al. (2007, cf. Eqn. 4). The surface properties (temperature and emissivity) and atmospheric profiles (temperature and specific humidity) in $\boldsymbol{b}$, and $\boldsymbol{x}_{\boldsymbol{a}}$ (e.g., upper level cloud top temperature for T_{ci}) are taken from the AIRS cloud-clearing product (L2 Standard file AIRX2RET for IR/MW and AIRS2RET for IR only). The averaging kernel matrix $\boldsymbol{A}$ quantifies the sensitivity of the retrieval with respect to changes in the true state:

$$\boldsymbol{A} = \boldsymbol{K}^{\boldsymbol{T}} \boldsymbol{S}_{\boldsymbol{\varepsilon}}^{-1} \boldsymbol{K} + \boldsymbol{S}_{\boldsymbol{a}}^{-1} \quad (2)$$

Scalar averaging kernels (AKs; ice_cld_opt_dpth_ave_kern, ice_cld_eff_diam_ave_kern, and ice_cld_temp_eff_ave_kern in L2 Support file) are reported for each of the three state vector retrieval parameters as off-diagonal terms of $\boldsymbol{A}$ in Eqn. (2) are not considered in K14. The scalar AKs quantify the information content of the retrieval with respect to $\boldsymbol{x}$. The normalized $\chi 2$ (ice_cld_fit_reduced_chisq in L2 Support file) is defined as:

$$\chi^2 = \frac{1}{N}\sum_{i=1}^{N}\left(\frac{y_i-[F(x)]_i}{\varepsilon_i}\right)^2 \quad , \tag{3}$$

where ε_i is the radiance error in channel i and N=59. The $\chi2$ from Eqn. (3) is calculated for 59 observed and simulated 8-14 μm channels (K14) and is used to determine the robustness of the radiance fits.

We have also tested the fidelity of r_{ei} within 6 K of the cold point tropopause. As AIRS observations are derived from IR thermal emission spectra, biases may arise in proximity to the tropopause. Any uncertainty in T_{ci}, the height and magnitude of the cold point tropopause, or temperature lapse rate may lead to increased uncertaintiy in r_{ei} as small spectral changes translate to large geophysical retrieval changes. Therefore, "filtered" sets of AIRS retrievals that remove ice clouds within 6 K of the cold point tropopause are shown throughout the paper, then are compared with "unfiltered" data when contrasted to DARDAR retrievals (see Section 6).

The average 14-year climatology of r_{ei}, τ_i, T_{ci}, and ice cloud frequency based on the IR only retrieval (AIRS2RET) is shown in Fig. 1. Retrievals with quality control (QC) flags QC=0 and QC=1 (K14; ice_cld_opt_dpth_QC, ice_cld_eff_diam_QC, and ice_cld_temp_eff_QC in L2 Support file) are included and the $\chi2$ is filtered using the QC flag specific to r_{ei}. The climatology is restricted to ice free ocean between 54°S–54°N as influences of surface heterogeneity including mountainous terrain, low emissivity such as bare mineral soils, and nocturnal and high latitude wintertime inversions on the ice parameter retrieval are not fully understood and warrant further investigation. A strict ad hoc QC may filter questionable data but the resulting data sample may skew the geophysical signals toward opaque clouds at the expense of transparent clouds that are more likely to be filtered out. The AIRS sensitivity is maximized for optically thinner cirrus with $\tau \leq 5$ (e.g., Huang et al., 2004), while MODIS sensitivity is maximized for optically thicker cirrus (e.g., Kahn et al., 2015; Chang et al., 2017).

The well-documented spatial distributions of ice clouds with maxima in the tropics and extratropical storm tracks and minima in the subtropical gyres are shown in Fig. 1. Higher magnitudes of r_{ei} are observed along the ITCZ where deep convection is more dominant, while a reduction is observed in the western Pacific Warm Pool region where transparent cirrus is more dominant. These patterns are consistent with previous observational and modelling studies. Yuan and Li (2010) found that MODIS r_{ei} is a few μm larger in tropical deep convection when compared to the extratropics for the same cloud top temperatures and T_bs. Barahona et al. (2014) show an increase in r_{ei} of a few μm in the Goddard Earth Observing System Model (GEOS-5) with improved comparisons against MODIS. Eidhammer et al. (2017) describe simulations using the Community Atmosphere Model (CAM5) for a consistent single ice species across cloud and precipitating ice hydrometeors without thresholds for autoconversion. A subtle but distinct double ITCZ is observed in the zonal averages, not unlike AIRS r_{ei} and τ_i in Fig. 1.

The loss of AMSU-A2 on 24 September 2016 led to the termination of the operational AIRS/AMSU combined infrared and microwave (AIRX2RET/AIRX2SUP) cloud clearing retrieval (Yue et al., 2017b). Since that time, the AIRS infrared only (AIRS2RET/AIRS2SUP) cloud clearing retrieval is the current operational version. The impacts of the loss of AMSU on retrieval parameters are assessed in great detail in Yue et al. (2017b). While many subtle changes were documented for vertical profiles of temperature and specific humidity, differences were more substantive for particular cloud properties. Further discussion regarding differences in Fig. 1 for AIRS2RET and AIRX2RET is found in the Appendix and shown in Fig. A1.

Figure 2 details AKs and χ^2 using identical QC as Fig. 1. Typically the AKs are much lower and the χ^2 fits much larger for QC=2 (not shown) and indicate lower information content and much poorer radiance fits. The AK and χ^2 patterns are spatially coherent and exhibit small variations between tropical convection, thin cirrus, and both extratropical storm tracks. The AKs have maxima on the equatorial side of the storm tracks with a poleward reduction and additional minima within the tropics. Multi-layer clouds are more frequent in the tropics and extratropical storm tracks (Chang and Li, 2005; Mace et al., 2009) and a reduction of the T_{ci} AKs in these areas is consistent with the single cloud layer assumption in the forward model (Kahn et al., 2015). However, the r_{ei} AK distributions strongly suggest that the single layer assumption is providing very high information content of ice cloud properties. Interestingly, the spatial patterns of r_{ei} AKs are correlated to τ_i (compare Figs. 1 and 2) in the low latitudes, where large values of τ_i align with slightly reduced r_{ei} AK. An area of reduction in the r_{ei} AK in the subtropical north Atlantic corresponds to the Saharan air layer. Generally χ^2 is about 3-4 between ±30° latitude with reductions in the ITCZ and extratropics. The spatial pattern of χ^2 does not closely track any of the AK patterns; thus for QC=[0,1] retrievals, spatial variations in information content do not correlate to the quality of the spectral fit. Differences between the IR/MW and IR only retrievals are generally minor but not negligible and are consistent with the loss of MW information. Further discussion regarding differences in Fig. 2 for AIRS2RET and AIRX2RET is found in the Appendix and depicted in Fig. A2.

2.2 AMSR-E/AMSR-2

Coincident satellite observations in the A-train are potentially valuable for gaining physical insight about the AIRS ice cloud properties. The Advanced Microwave Sounding Unit–Earth Observing System (AMSR-E) on Aqua and AMSR-2 instrument on GCOM-W1 are used to determine several atmospheric and surface properties that coincide with AIRS. The AMSR-E instrument was operational from 4 May 2002 until 4 October 2011, while AMSR-2 is currently operational since 18 May 2012. We focus on the summer months July and August from 2003–2016 in this investigation. The total column water vapour (CWV) cloud liquid water path (CWP), rain rate (RR) (Hilburn and Wentz, 2008), sea surface temperature (T_{sfc}) (Gentemann et al., 2010), and direction-independent near surface wind speed (u) are obtained from AMSR-E (Wentz et al., 2014a) and AMSR-2 (Wentz et al., 2014b) using Version 7 data.

2.3 DARDAR

We use the CloudSat, CALIPSO, and MODIS radar/liDAR (DARDAR) combined ice cloud property retrieval developed by Delanoë and Hogan (2008; 2010) to investigate r_{ei} in a variety of ice clouds. This algorithm is based on an OE algorithm that includes CALIOP's lidar backscatter and CloudSat's radar reflectivity to retrieve vertical profiles of IWC, r_{ei}, and other

Atmos. Chem. Phys. Discuss., https://doi.org/10.5194/acp-2017-1216
Manuscript under review for journal Atmos. Chem. Phys.
Discussion started: 31 January 2018

Atmospheric Chemistry and Physics Discussions

cloud variables. The ice cloud property retrievals are available at CloudSat's 1.4 km horizontal resolution and CALIPSO's 60 m vertical resolution and are matched to the nearest AIRS pixel. As the radar and lidar have different sensitivities to a range of cloud characteristics, the retrieval is functional when one of the instruments is unable to detect clouds either because of small ice particles or strong attenuation. Deng et al. (2013) showed that there is very good agreement in r_{ei} between DARDAR, 2C-ICE, and in situ obtained observations from the Small Particles in Ice (SPARTICUS) field campaign; therefore only DARDAR data is used in this study.

DARDAR contains two products: DARDAR-MASK (Delanoë and Hogan, 2010; Ceccaldi et al., 2013) and DARDAR-CLOUD (Delanoë and Hogan, 2008, 2010), which are both available through the ICARE Thematic Center (http://www.icare. univ-lille1.fr/drupal/archive/). DARDAR-MASK provides the vertical cloud classification and a range of additional categorizations (e.g., clear, aerosols, rain, supercooled and warm liquid, mixed phase, ice). DARDAR-CLOUD provides ice cloud properties such as extinction, r_{ei}, and IWC by a variational radar-lidar ice-cloud retrieval algorithm called VarCloud (Delanoë and Hogan, 2008). In this product, normalized ice particle size distributions are used and non-spherical particles leverage in situ measurements (Delanoë et al., 2014).

3 Methodology

3.1 Pixel matching

A pixel scale nearest neighbour matching approach (Fetzer et al., 2013) is applied to AIRS/AMSU, AMSR-E and AMSR-2 from 01 September 2002 until 31 August 2016. By retaining the native spatial and temporal covariances in the matched data, smaller scale and faster temporal processes are captured that are otherwise lost to spatial gridding and temporal averaging (e.g., Kahn et al., 2017). The same methodology is applied between AIRS/AMSU and DARDAR from 01 July 2006 until 31 December 2008 within the subset of AIRS/AMSU pixels along the CloudSat-CALIPSO ground track.

3.2 Secular trends

Trends and their statistical significance are calculated following Santer et al. (2000) using a two-sided t-test and confidence intervals at the 95% significance level. The 95% confidence intervals are also calculated for a lag-1 autocorrelation in order to assess the sensitivity to highly correlated time series (Cressie, 1980; Santer et al., 2000). Trends are calculated for two different spatial averages. First, global monthly anomalies at 1°×1° resolution over the 14-year observing period are calculated then trends are reported at the same spatial resolution. Second, monthly anomalies averaged between 54°S–18°S, 18°S–18°N, and 18°S–54°N are calculated then trends with 95% confidence intervals with and without lag-1 autocorrelation are determined and displayed as box and whisker diagrams. Three sets of AIRS properties are described: combined IR/MW, IR only, and IR only for the 1/3 of pixels in the swath nearest to nadir view. The purpose of contrasting results between IR only and combined IR/MW is to highlight differences between the two algorithms with further detail found in the Appendix. The purpose of showing near nadir IR only is to demonstrate the overall lack of sensitivity in the results to scan angle.

3.3 Joint histograms

Instantaneous pixel matches of AMSR-E and AMSR-2 variables versus AIRS ice cloud properties are used to construct joint histograms following the approach described in Kahn et al. (2017). The joint histograms contain the natural log of counts with r_{ei} contours superimposed. The intent of these diagrams is to reveal the physical response of cloud top r_{ei} to precipitating and non-precipitating cloud types and meteorological variability. The emphasis is on r_{ei} versus T_{ci} to facilitate comparisons with previous works that describe temperature dependence of r_{ei}.

3.4 Comparing DARDAR and AIRS r_{ei}

The retrievals of r_{ei} from AIRS and DARDAR are compared in single-layer cirrus and convective clouds over ocean. We use the CloudSat reflectivity, DARDAR-MASK, and DARDAR-CLOUD products to define cirrus only (Ci), cirrus above weak convection (Weak Conv), and cirrus above strong convection (Strong Conv). We begin with identifying the number of cloud layers in each profile and the cloud top height (CTH) and cloud bottom height (CBH) of each layer. Profiles with more than three layers of clouds are not included in the statistics. Cirrus is defined as CBH>12km (e.g., Keckhut et al., 2006), and deep convection is defined as CTH>10km and CBH<2km (Takahashi and Luo, 2014). Among deep convective clouds, weak and strong convection are defined by the echo top height (ETH) of the 10 dBZ contour: the ETH of 10dBZ>10km (Luo et al, 2008; Takahashi and Luo, 2012, 2017) for strong deep convection, while the ETH at 10dBZ<5km for weak deep convection. For the statistics described later, the upper layer cirrus is chosen to have 1) CTH<tropopause height, 2) cloud base temperature<200K, and cirrus geometrical thickness <1km.

4 Results

4.1 Global trends

The 14-year temporal trends in the cloud properties depicted in Fig. 1 are shown in Fig. 3. The T_{ci} decreases about 1–2 K in most areas, but a few regions are found to increase. The trend in r_{ei} is increasing nearly everywhere, from a few tenths to 1–2 μm, with the largest values in proximity to tropical convection. While the upward trend in r_{ei} is somewhat noisy at 1°×1°, the increase is notably consistent across the global oceans. In contrast, τ_i is decreasing in most regions except for convectively active regions in the ITCZ, parts of the tropical western Pacific Warm Pool, and southern Indian Ocean. The trend in ice frequency is similar to τ_i but is spatially smoother and the magnitude is much larger in the tropics.

Trends in the AKs and χ^2 are shown in Fig. 4. Generally speaking, the trends in the retrieval parameters do not resemble the spatial patterns of trends in their respective AKs. The trends for r_{ei} AKs in Fig. 4 resemble τ_i trends in Fig. 3. This shows that the information content of r_{ei} changes with respect to trends in τ_i. The trends for r_{ei} however do not resemble trends in either τ_i or τ_i AKs. We conclude that the upward trend in r_{ei} is independent of the gain or loss of information in r_{ei}. The trends in χ^2 are quite subtle and are smallest when the ice frequency is largest. There is an increased zonal symmetry in the T_{ci} AK trend than the T_{ci} trend in Fig. 3 and no obvious correspondence is apparent between the sign of the T_{ci} trend in Fig. 3 and the T_{ci} AK trend in Fig. 4. The τ_i AK trend is generally upwards except in a few tropical locations including the Saharan air layer. The spatial patterns in τ_i AK trends do not appear to be related to other fields. In conclusion, the observed trends in the ice cloud properties in Fig. 3 do not appear to be caused by the gain or loss of information content, or the fidelity of the radiance fitting in the retrieval.

4.2 Latitude bands

The anomaly time series of r_{ei} for three latitude bands and the IR/MW, IR only, and IR nadir retrievals are shown in Fig. 5. While the anomaly time series for most of the 1°×1° grid boxes are not statistically significant (not shown), a statistically significant signal is obtained for the broad oceanic latitude bands. The strong similarity in the anomaly time series for IR/MW, IR only, and IR nadir is apparent for r_{ei} and is also true for the other variables (not shown). Despite some of the regional spatial differences in IR/MW and IR only retrievals described in the Appendix, the algorithm differences are miniscule with regard to the anomaly time series.

Figure 6 summarizes the results for three latitudinal bands and IR/MW, IR only, and IR nadir for 95% confidence intervals with and without lag-1 autocorrelation. The extratropical SH and NH upward trends in r_{ei} (Fig. 6b) are steadier with time than the tropics, which appears initially flat but then jumps upwards since 2013 (Fig. 5); however all three regions and retrievals exhibit statistically significant trends (Fig. 6). The T_{ci} trends (Fig. 6a) show about 0.5–1.0 K of cooling for the three latitude bands and three data sets, with IR nadir exhibiting 95% confidence except for the lag-1 autocorrelation. The τ_i trends (Fig. 6c) are downward by 0.025–0.075 (significant at 95% in the SH and NH, not so in the tropics). The AKs are slightly downwards for T_{ci} (Fig. 6d) and r_{ei} (Fig. 6e) and upwards for τ_i (Fig. 6f); there is a mix of statistical significance that depends on the retrieval algorithm and latitude band. The χ^2 trends (Fig. 6h) are essentially not statistically significant except for IR nadir in the tropics. Ice frequency (Fig. 6g) decreases by about 1% with respect to all AIRS pixels in the SH and NH extratropics (significant at 95%) and much less so in the tropics (not significant at 95%). Lastly, the IWP (Fig. 6i) decreased about 0.4–0.8 g m^{-2} in the SH (marginal significance at 95%) and NH (significant at 95%), and increased about 0.25 g m^{-2} in the tropics (not significant at 95%). This latitudinal pattern is similar to the CMIP5 zonal average ensemble mean (Ceppi et al., 2016; cf. Fig. 1c) although the reduction of AIRS IWP appears larger in magnitude than CMIP5 IWP. The statistical significance of IWP is reduced, however, when compared to τ_i because of the compensating increases in r_{ei} at all latitudes.

4.3 Potential impacts from radiometric drift

While the radiometric stability of AIRS is established to be approximately 4 ±1 mK yr^{-1} (Pagano et al., 2012), the impacts of radiometric drift on secular cloud property trends has not been assessed to date. Two different tests have been designed to estimate the effects on the cloud products: (1) add +50 mK to all 59 cloud retrieval channels in K14 after cloud clearing but before the ice cloud property retrieval, and (2) add +50 mK to cloud clearing channels and K14 channels but before cloud clearing is performed. Experiment (1) isolates radiometric drift on ice cloud properties only, while (2) accounts for impacts from the full physical retrieval. Manning and Aumann (2017) raise the possibility of channel-dependent drift that could cause a systematic change in slope in the 8–14 μm region for T_b < 200 K; however these effects are subtle and are undetermined (but likely much smaller) for warmer brightness T_bs that dominate the vast majority of AIRS pixels. Further investigation into radiometric drift scenarios on the AIRS Level 2 retrieval system is warranted.

The results of the two experiments are summarized in Table 1 for one day of retrievals on 6 September 2002 for ±54° latitude over the oceans and for QC=[0,1]. Both experiments indicate that differences with respect to the IR/MW retrieval are substantially smaller than the trends reported in this study. For the experiments before and after cloud clearing, Δr_{ei} is -0.13 and -0.1 μm, $\Delta\tau_i$ is +0.01 and +0.005, and ΔT_{ci} is +0.24 and +0.26 K, respectively. The AK trends for cloud variables for the perturbation experiments are much less than depicted in Fig. 6. In summary, the two simple radiance perturbation experiments fall well short of explaining the magnitude of the observed ice property trends, although some fractional contribution to observed trends cannot be ruled out.

5 Insight into convective processes with AMSR

Using ground-based retrievals at Darwin, Protat et al. (2011) found that r_{ei} is ~1–3 μm larger during active deep convection compared to suppressed conditions. Using a simultaneous retrieval of ice cloud properties from the MODIS and POLDER instruments, van Diedenhoven et al. (2014) found that r_{ei} is larger in stronger convective events compared to others at a given cloud top pressure. van Diedenhoven et al. (2016) used in situ aircraft observations to show that r_{ei} decreases with height, reaches a minimum around 14 km, and may subsequently increase at higher altitudes. Barahona et al. (2014) obtained an increase of a few μm for clouds colder than 195 K with GEOS-5 and Hong and Liu (2015) show similar results with DARDAR data for the thickest convective clouds above 10 km. Convective overshoots into the lower stratosphere are 0.3–4.0 μm larger than non-overshooting deep convection observed with DARDAR data (Rysman et al., 2017). Lawson et al. (2010) use in situ aircraft probe data of ice particles in aged cirrus in proximity to convection to show that particle size is more weakly dependent on temperature below 215 K. These previous investigation help motivate the joint histograms that follow.

5.1 Differences in r_{ei} between opaque and transparent clouds

We show separate vertical profiles of AIRS r_{ei} with T_{ci} for transparent and opaque clouds in Fig. 7. Effective cloud fraction (ECF) with a cut-off of 0.98 (Protopapadaki et al., 2017) is used to categorize the two types (transparent with ECF < 0.98 and opaque with ECF ≥ 0.98). Approximately 9.4% of cloud tops are identified as opaque and 90.6% are transparent. Opaque and transparent clouds are further subdivided into three categories using AMSR-E/AMSR-2 CWP and RR: no cloud or rain (CWP=0 and RR=0), cloud but no rain (CWP>0 and RR=0), and cloud with rain (CWP>0 and RR>0). Symbols show mean r_{ei} over 10 K bins derived from IWC and extinction observations for three tropical in situ field campaigns: the Cirrus Regional Study of Tropical Anvils and Cirrus Layers–Florida Measurements for Area Cirrus Experiment (CRYSTAL-FACE, diamonds), the Tropical Composition, Cloud, and Climate Coupling Experiment (TC4, triangles), and the NASA African Monsoon Multidisciplinary Analysis (NAMMA, squares) campaigns (e.g., Heymsfield et al., 2014).

A maximum r_{ei} occurs near 230 K and decreases at warmer and colder T_{ci} for transparent clouds in the tropics (Fig. 7). About 21.6% of cases are clear according to AMSR but cloudy according to AIRS. About 60.7% have CWP>0 and RR=0. Both of these categories have nearly identical T_{ci} dependence. The remaining 17.8% have CWP>0 and RR>0, and r_{ei} is 1.5-2.5 μm larger than no rain, with the largest differences for T_{ci} <210K. For opaque clouds in the tropics, r_{ei} is substantially larger for all T_{ci} than transparent clouds. There is more than double the relative frequency of occurrence with raining opaque clouds compared to raining transparent clouds. Except for CWP=0 and RR=0, a consistent increase in r_{ei} is found for increasing T_{ci}. A flattening in the reduction in r_{ei} for T_{cld} <210K occurs and is similar to the results of van Diedenhoven et al. (2016). While this region is sensitive to the 6 K cut-off used to filter questionable retrievals near the tropopause, the profile in Fig. 7b is robust for ~4 K and larger. While the in situ r_{ei} estimates are somewhat larger for T_{ci} > 220 K, this is expected as these observations may be obtained well below cloud top in which the infrared signal is not sensitive. Furthermore, the 1-sigma variability of the in situ observations (not shown) has a magnitude that is approximately as large as the AIRS estimates of 1-sigma, providing significant overlap between satellite and in situ observations.

5.2 Dependence of r_{ei} on near surface wind speed

Correlations between rain rate and near surface wind speed in passive MW observations have been previously shown to indicate a tropical precipitation-convergence feedback (Back and Bretherton, 2005). The AMSR low frequency (LF) wind is used to quantify the response of r_{ei} to variability in near surface wind speeds in the presence of convection. Figure 8 shows that opaque clouds exhibit strong dependence on wind speed; the weakest (strongest) winds are associated with the largest (smallest) r_{ei}. The reduction in r_{ei} is ~2 μm for T_{ci}<210K but can be as large as 10–12 μm for T_{ci}>230 K. The dependence for transparent clouds is of opposite sign and lower magnitude when compared to opaque clouds. Figures 8a,b are also calculated with NWP model winds and are nearly identical with <1 μm difference (not shown). The consistency with NWP winds provided confidence in partitioning them into the individual u- and v-components and the u-component is shown in Fig. 8c,d. The largest values of r_{ei} are found for light easterly winds around 5 m s^{-1}, consistent with convectively active regimes generating larger r_{ei} (e.g., Protat et al., 2011). Smaller values of r_{ei} are associated with westerly winds during suppressed convection. Changes in r_{ei} due to wind direction changes are largest for T_{ci}>230K and are lowest for the coldest convective cloud tops. The opposite is found for transparent clouds but for smaller values of 1–4 μm with a maximum near T_{ci}=230 K. As discussed previously, the order of magnitude larger sample size for transparent clouds overwhelm those for opaque clouds; therefore dependence of r_{ei} on convection would be obscured if clouds were not partitioned by opacity.

5.3 Dependence of r_{ei} on CWV and T_{sfc}

The T_{sfc} and CWV also correlate to r_{ei} (Fig. 9a,b). Opaque clouds exhibit a 2–8 μm jump as CWV increases from 45-65 mm, with the largest values for T_{ci}>230K; a similar pattern is observed for T_{sfc} (Fig. 9c,d). While the results are similar for transparent clouds, the increase with CWV is muted to 1–4 μm and is shifted to CWV>60 mm; r_{ei} does not exhibit a relationship with T_{sfc} in transparent clouds. Overall the r_{ei} is lower in transparent clouds compared to opaque clouds for all combinations of T_{ci}, CWV, and T_{sfc}.

6 Comparisons of AIRS and DARDAR r_{ei}

In the previous section, we showed that AIRS observes larger r_{ei} at the tops of convection with respect to variations in surface wind speed, T_{sfc}, CWV and precipitation rate. In this section, the r_{ei} at the base of single-layer cirrus clouds, cirrus clouds above weak deep convection, and cirrus clouds above strong deep convection will be shown separately using the classification defined in Section 3.4. Stephens (1983) argued for a radiative mechanism that leads to r_{ei} growth in cirrus overlying lower-layer clouds from enhanced radiative cooling; particle growth (decay) occurs in a radiatively cooled (heated) environment. DARDAR data is used to test whether the mechanism of Stephens (1983) is operating in observations, and also to determine the behaviour of AIRS in the same clouds. As opacity increases, or the higher (colder) the lower layer cloud occurs, the cooling from the cirrus layer is enhanced and larger r_{ei} should therefore be observed. Systematic changes in the global circulation and changes in convective clustering and cloud overlap may lead to a higher frequency of overlapping cirrus on top of convection, and a reduced frequency of single-layered cirrus with climate change. Thus, we want to determine if this is a viable mechanism that contributes to upward trends in r_{ei}.

Figure 10 shows the median (centre lines), mean (asterisks), and interquartile range (bottom and top edges of boxes) for DARDAR, IR/MW, and IR only AIRS retrievals, with filtered (non-filtered) versions of IR/MW and IR only that have retrievals within 6 K of the cold point tropopause removed (retained). For single-layer cirrus (Ci), AIRS is typically 2-3 μm larger than DARDAR with about 1 μm difference between IR/MW and IR only. For cirrus above weak convection (Weak Conv), AIRS remains about 2-3 μm larger than DARDAR as all AIRS retrievals increase about 2-3 μm in the mean compared to single-layer cirrus. For cirrus above strong convection (Strong Conv), the differences between DARDAR and AIRS are reduced, with IR only about 1-1.5 μm larger than IR/MW. The width of the DARDAR quantiles increases from single-layer cirrus to cirrus over strong convection indicating increased variability in r_{ei}; AIRS and DARDAR have nearly identical variability for cirrus above strong convection. AIRS and DARDAR exhibit an increase in r_{ei} as convective cloud appears below cirrus layers suggesting that the mechanism described in Stephens (1983) may be operating in these differences. Differentiating the increase in r_{ei} from the Stephens (1983) radiative cooling mechanism for particle growth, and lofting of large ice particles from adjacent convection, however, cannot be easily differentiated; further investigation is warranted in the context of r_{ei} trends shown in this work.

7 Summary and Conclusions

While high-level ice clouds are a key component of the changing climate system, there remains an absence of well-characterized observational constraints of ice cloud microphysics that are desired for climate model evaluation (Kärcher, 2017). The Atmospheric Infrared Sounder (AIRS) instrument, launch in May of 2002, has an excellent radiometric stability of ±3-4 mK yr^{-1} (Pagano et al., 2012). We use the AIRS version 6 ice cloud property and thermodynamic phase retrievals (Kahn et al., 2014) to quantify variability and trends in ice cloud frequency, ice cloud top temperature (T_{ci}), ice optical thickness (τ_i) and ice effective radius (r_{ei}) from 01 September 2002 until 31 August 2016. We also investigate the scalar averaging kernels (AKs) associated with each retrieval quantity to determine changes in information content; and the χ^2 fitting parameter, which quantifies the fidelity of the observed and simulated radiance fits across cloud types. Differences are described between in the ice cloud properties using the AIRS/AMSU combined cloud-clearing retrieval (IR/MW), the AIRS only cloud-clearing retrieval (IR only), and a subset of IR only for the 1/3 of pixels nearest to nadir view (IR nadir).

Spatial patterns in r_{ei} reflect differences in proximity to deep convection, thin cirrus, and extratropical storm tracks. The averaging kernels and χ^2 patterns are spatially coherent and exhibit variations between different cloud regimes with slight variations observed. The spatial patterns of χ^2 and averaging kernels do not resemble each other; for the highest quality retrievals, we can conclude that the spatial variations in information content do not correlate to the spectral radiance fit in the retrievals of Kahn et al. (2014). The trends are nominally 1–2 K of cooling in T_{ci}, an increase of a few tenths to ~1 µm in r_{ei}, with the largest values in proximity to tropical convection. In contrast, τ_i is decreasing except for regions with high frequencies of convection (ITCZ, W. Pacific Warm Pool, and S. Indian Ocean). The trend in ice frequency is similar to τ_i but is spatially smoother and the magnitude is much larger.

The statistical significance of three wide latitude bands in the tropics, SH, and NH extratropics are calculated following the methodology of Santer et al. (2000). Ice frequency decreases by about 1% with respect to all AIRS pixels in the SH and NH extratropics (significant at 95%), and much smaller in the tropics (not significant at 95%). The ice water path (IWP) decreases by 0.4–0.8 g m^{-2} in the SH (marginal significance at 95%) and NH (significant at 95%), and increases about 0.25 g m^{-2} in the tropics (not significant at 95%). The statistical significance of IWP is lower than τ_i because of compensating increases in r_{ei} at all latitudes (significant at 95%). Impacts of assumed radiometric drift on cloud property trends were determined for a few perturbation experiments. The perturbation experiments fall significantly short of explaining the magnitude of the observed ice property, AKs, and χ^2 trends, although some fractional contribution to trends cannot be ruled out.

Surface based and aircraft in situ observations have demonstrated that active periods of deep convection are associated with larger r_{ei} at cloud top (e.g., Protat et al.; 2011; van Diedenhoven et al., 2014). AIRS r_{ei} are plotted against T_{ci} for transparent and opaque clouds separately; approximately 9.4% of cloud tops are identified as opaque and 90.6% are transparent. Values of r_{ei} are substantially larger for all T_{ci} within opaque clouds that are a proxy for deep convection. A reduction in the dependence of r_{ei} with T_{ci} <210K occurs and shows similarity to van Diedenhoven et al. (2016). Opaque clouds exhibit strong dependence on wind speed; the weakest (strongest) winds are associated with the largest (smallest) r_{ei} with differences as large as 10–12 μm. Opaque clouds exhibit a 2–8 μm jump as CWV increases from 45-65 mm, and a similar pattern is observed for T_{sfc}. Transparent clouds exhibit a 1–4 μm jump that is shifted to CWV>60 mm; while no relationship between r_{ei} and T_{sfc} is observed.

Comparisons between DARDAR and AIRS r_{ei} are made for single-layer cirrus, cirrus above weak convection, and cirrus above strong convection. AIRS is typically 1-3 μm larger than DARDAR with about 1 μm difference between IR/MW and IR only. AIRS and DARDAR exhibit an increase in r_{ei} as convective cloud appears below cirrus layers suggesting that the mechanism described in Stephens (1983) may be operating in these differences. However, secular trends in convective aggregation, convective mode, the probability distribution of vertical velocity, and ice nucleation and growth mechanisms that may change within the changing character of convection (e.g., Chen et al., 2016), are highly complex and uncertain in observations. Further research is necessary to quantify the links between trends in ice cloud microphysics shown in this work with cloud responses in climate model simulations.

Appendix

Figure A1 shows that the AIRS algorithm differences in IR only (AIRS2RET) minus IR/MW (AIRX2RET) on the frequency of ice phase clouds over the global oceans are less than 1%. This implies that virtually the same sets of pixels are identified as ice in the two retrievals. The impacts on T_{ci} are on the order of 1–2 K difference with IR only slightly cooler especially in the tropics. Some subtle and spatially coherent changes in τ_i of ~0.1 are observed with IR only thinner. The r_{ei} is larger by 0.5–1.0 μm in IR only compared to IR/MW but a few of the extratropical storm track regions exhibit an opposite sign. To summarize, for the IR only retrieval, τ_i is lower by 0.1, r_{ei} is larger by 0.5–1.0 μm in most areas, and T_{ci} is lower by 1–2 K depending on the latitude.

Figure A2 shows the same differences as Fig. A1, except for the T_{ci}, r_{ei}, and τ_i AKs, and the χ^2 fitting parameter. The differences in AKs and χ^2 are generally small but some notable regional differences are observed. The T_{ci} AK is mostly lower for the IR only compared to IR/MW and is consistent with added information provided by the microwave channels in the AMSU instrument. The r_{ei} AK is larger for the IR only compared to IR/MW but the difference is an order of magnitude smaller than the T_{ci} AK difference. The τ_i AK difference is small and does not exhibit coherent cloud-regime dependence except for the Saharan air layer. The difference in χ^2 shows slightly worse fitting for the IR only; this is also consistent with added information provided by microwave channels in the AMSU instrument. Most of the globe is 0.1–0.2 higher for IR only, which is about 5% of the mean value of χ^2=3-4 for retrievals restricted to QC=[0,1].

Acknowledgments

AMSR-E and AMSR-2 data products are produced by Remote Sensing Systems and were sponsored by the NASA AMSR-E Science Team, and all data are available through www.remss.com. The collocation methodology matching AIRS/AMSU with AMSR-E/AMSR-2 and DARDAR was facilitated by the use of index files generated through the NASA Earth Science Program NASA's Making Earth Science Data Records for Use in Research Environments (MEaSUREs) program. DARDAR-MASK and DARDAR-CLOUD are both available through the ICARE Thematic Center (http://www.icare. univ-lille1.fr/drupal/archive/). AIRS data were obtained through the Goddard Earth Services Data and Information Services Center (http://daac.gsfc.nasa.gov/). Brian H. Kahn was partially supported by the AIRS project at JPL and by the NASA Science of Terra and Aqua program under grant NNN13D455T. Part of this research was carried out at the Jet Propulsion Laboratory (JPL), California Institute of Technology, under a contract with the National Aeronautics and Space Administration.

Data citation

Fetzer, E., Wilson, B., and Manipon, G.: AIRS-AMSU variables-CloudSat cloud mask, radar reflectivities, and cloud classification matchups V3.2, Greenbelt, MD, USA, Goddard Earth Sciences Data and Information Services Center (GES DISC), doi:10.5067/MEASURES/WVCC/DATA201, 2013.

Teixeira, J.: AIRS/Aqua L2 Standard Physical Retrieval (AIRS+AMSU) V006, Greenbelt, MD, USA, Goddard Earth Sciences Data and Information Services Center (GES DISC), 10.5067/AQUA/AIRS/DATA201, 2013.

Wentz, F. J., T. Meissner, T., Gentemann, C., Brewer, M.: Remote Sensing Systems AQUA AMSR-E Daily Environmental Suite on 0.25 deg grid, Version V7. Remote Sensing Systems, Santa Rosa, CA. Available online at www.remss.com/missions/amsr, 2014. [Accessed 16 May 2017]

Wentz, F.J., Meissner, T., Gentemann, C., Hilburn, K. A., and Scott, J.: Remote Sensing Systems GCOM-W1 AMSR2 Daily Environmental Suite on 0.25 deg grid, Version V7.2. Remote Sensing Systems, Santa Rosa, CA. Available online at www.remss.com/missions/amsr, 2014. [Accessed 17 Jul 2017]

References

Back, L. E., and Bretherton, C. S.: The relationship between wind speed and precipitation in the Pacific ITCZ, J. Climate, 18, 4317–4328, 2005.

Barahona, D., Molod, A., Bacmeister, J., Nenes, A., Gettelman, A., Morrison, H., Phillips, V., and Eichmann, A.: Development of two-moment cloud microphysics for liquid and ice within the NASA Goddard Earth Observing System Model (GEOS-5), Geosci. Model Dev., 7, 1733–1766, 2014.

Baum, B. A., Yang, P, Nasiri, S. L., Heidinger, A. K., Heymsfield, A. J., and Li, J.: Bulk scattering properties for the remote sensing of ice clouds. Part III: High-resolution spectral models from 100 to 3250 cm^{-1}, J. Appl. Meteorol. Climatol., 46, 423–434, 2007.

Baumgardner, D., Abel, S. J., Axisa, D., Cotton, R., Crosier, J., Field, P., Gurganus, C., Heymsfield, A., Korolev, A., Krämer, M., Lawson, P., McFarquhar, G., Ulanowski, Z., and Um, J.: Chapter 9. Cloud ice properties: In situ measurement challenges, Met. Monographs, 9.1–9.23, doi:10.1175/AMSMONOGRAPHS-D-16-0011.1, 2017.

Bender, F. A. M., Ramanathan, V., and Tselioudis, G.: Changes in extratropical storm track cloudiness 1983–2008: Observational support for a poleward shift, Clim. Dyn., 38, 2037–2053, 2012.

Bony, S., Stevens, B., Coppin, D., Becker, T., Reed, K. A., Voigt, A., and Medeiros, B.: Thermodynamic control of anvil cloud amount, Proc. Natl. Acad. Sci., 113(32), 8927–8932, doi:10.1073/pnas.1601472113, 2016.

Ceccaldi, M., Delanoë, J., Hogan, R. J., Pounder, N. L., Protat, A., and Pelon, J.: From CloudSat-CALIPSO to EarthCare: Evolution of the DARDAR cloud classification and its comparison to airborne radar-lidar observations, J. Geophys. Res. Atmos., 118, 7962–7981, doi:10.1002/jgrd.50579, 2013.

Chang, F. L. and Li, Z.: A near global climatology of single-layer and overlapped clouds and their optical properties retrieved from TERRA/MODIS data using a new algorithm, J. Clim., 18, 4752–4771, 2005.

Chang, K.-W., L'Ecuyer, T. S., Kahn, B. H., and Natraj, V.: Information content of visible and midinfrared radiances for retrieving tropical ice cloud properties, J. Geophys. Res. Atmos., 122, 4944–4966, doi:10.1002/2016JD026357, 2017.

Chen, Y.-W., Seiki, T., Kodama, C., Satoh, M., Noda, A. T., and Yamada, Y.: High cloud responses to global warming simulated by two different cloud microphysics schemes implemented in the Nonhydrostatic Icosahedral Atmospheric Model (NICAM), J. Climate, 29, 5949–5964, 2016.

Cressie, N.: Relaxing assumptions in the one sample t-test, Australian J. Stat., 22(2), 143–153, 1980.

Delanoë, J., and Hogan, R. J.: A variational scheme for retrieving ice cloud properties from combined radar, lidar, and infrared radiometer, J. Geophys. Res., 113, D07204, doi:10.1029/2007JD009000, 2008.

Delanoë, J., and Hogan, R. J.: Combined CloudSat-CALIPSO-MODIS retrievals of the properties of ice clouds. J. Geophys. Res., 115, D00H29, doi:10.1029/2009JD012346, 2010.

Delanoë, J., Heymsfield, A. J., Protat, A., Bansemer, A., and Hogan, R. J.: Normalized particle size distribution for remote sensing application, J. Geophys. Res. Atmos., 119, 4204-4227, doi:10.1002/2013JD020700, 2014.

Deng, M., Mace, G. G., Wang, Z., and Lawson, R. P.: Evaluation of several A-train ice cloud retrieval products with in situ measurements collected during the SPARTICUS campaign, J. Appl. Meteor. Climatol., 52, 1014–1030, 2013.

Dim, J. R., Murakami, H., Nakajima, T. Y., Nordell, B., Heidinger, A. K., and Takamura, T.: The recent state of the climate: Driving components of cloud-type variability, J. Geophys. Res., 116, D11117, doi:10.1029/2010JD014559, 2011.

Eidhammer, T., Morrison, H., Mitchell, D., Gettelman, A., and Erfani, E.: Improvements in global climate model microphysics using a consistent representation of ice particle properties, J. Climate, 30, 609–629, 2017.

Fan, J., Leung, L. R., Rosenfeld, D., Chen, Q., Li, Z., Zhang, J., and Yan, H.: Microphysical effects determine macrophysical response for aerosol impacts on deep convective clouds, P. Natl. Acad. Sci., 110, E4581–E4590, 2013.

Fauchez, T., Dubuisson, P., Cornet, C., Szczap, F., Garnier, A., Pelon, J., and Meyer, K.: Impacts of cloud heterogeneities on cirrus optical properties retrieved from space-based thermal infrared radiometry, Atmos. Meas. Tech., 8, 633–647, https://doi.org/10.5194/amt-8-633-2015, 2015.

Garnier, A., Pelon, J., Dubuisson, P.,Yang, P., Faivre, M., Chomette, O., Pascal, N., Lucker, P., and Murray, T.: Retrieval of cloud properties using CALIPSO Imaging Infrared Radiometer, Part II: effective diameter and ice water path, J. Appl. Meteorol. Climatol., 52, 2582–2599, doi:10.1175/JAMC-D-12-0328.1, 2013.

Gentemann, C. L., Meissner, T., and Wentz, F. J.: Accuracy of Satellite Sea Surface Temperatures at 7 and 11 GHz, IEEE Trans. Geosci. Remote Sens., 48, 1009–1018, 2010.

Gettelman, A., Liu, X., Ghan, S. J., Morrison, H., Park, S., Conley, A. J., Klein, S. A., Boyle, J., Mitchell, D. L., and Li, J.-L. F.: Global simulations of ice nucleation and ice supersaturation with an improved cloud scheme in the Community Atmosphere Model, J. Geophys. Res., 115, D18216, doi:10.1029/2009JD013797, 2010.

Grabowski, W. W.: Untangling Microphysical Impacts on Deep Convection Applying a Novel Modeling Methodology, J. Atmos. Sci., 72, 2446–2464, 2015.

Hilburn, K. A., and Wentz, F. J.: Intercalibrated Passive Microwave Rain Products from the Unified Microwave Ocean Retrieval Algorithm (UMORA), J. Appl. Meteor. Climatol., 47, 778–794, 2008.

Hong, Y. and Liu, G.: The characteristics of ice cloud properties derived from CloudSat and CALIPSO measurements, J. Climate, 28, 3880–3901, 2015.

Huang, H.-L., Yang, P., Wei, H., Baum, B. A., Hu, Y., Antonelli, P., and Ackerman, S. A.: Inference of ice cloud properties from high spectral resolution infrared observations, IEEE Trans. Geosci. Remote Sens., 42, 842–853, 2004.

Irion, F. W., Kahn, B. H., Schreier, M. M., and Coauthors: Single-footprint retrievals of temperature, water vapor and cloud properties from AIRS, Atmos. Meas. Tech. Discuss., https://doi.org/10.5194/amt-2017-197, 2017.

Jiang, J. H., Su, H., Zhai, C., Massie, S. T., Schoeberl, M. R., Colarco, P. R., Platnick, S., Gu, Y., and Liou, K.-N.: Influence of convection and aerosol pollution on ice cloud particle effective radius, Atmos. Chem. Phys., 11, 457–463, 2011.

Jin, H. and Nasiri, S. L.: Evaluation of AIRS cloud-thermodynamic phase determination with CALIPSO, J. Appl. Meteor. Climatol., 53, 1012–1027, 2014.

Kahn, B. H., Liang, C. K., Eldering, A., Gettelman, A., Yue, Q., and Liou, K. N.: Tropical thin cirrus and relative humidity observed by the Atmospheric Infrared Sounder, Atmos. Chem. Phys., 8, 1501–1518, doi:10.5194/acp-8-1501-2008, 2008.

Kahn, B. H., Irion, F.W., Dang, V. T., Manning, E. M., Nasiri, S. L., Naud, C. M., Blaisdell, J. M., Schreier, M. M., Yue, Q., Bowman, K. W., Fetzer, E. J., Hulley, G. C., Liou, K. N., Lubin, D., Ou, S. C., Susskind, J., Takano, Y., Tian, B., and Worden, J. R.: The Atmospheric Infrared Sounder version 6 cloud products, Atmos. Chem. Phys., 14, 399–426, https://doi.org/10.5194/acp-14-399-2014, 2014.

Kahn, B. H., Schreier, M. M., Yue, Q., Fetzer, E. J., Irion, F. W., Platnick, S., Wang, C., Nasiri, S. L., and L'Ecuyer, T. S.: Pixel-scale assessment and uncertainty analysis of AIRS and MODIS ice cloud optical thickness and effective radius, J. Geophys. Res.-Atmos., 120, 11669–11689, 2015.

Kahn, B. H., Matheou, G., Yue, Q., Fauchez, T., Fetzer, E. J., Lebsock, M., Martins, J., Schreier, M. M., Suzuki, K., and Teixeira, J.: An A-train and MERRA view of cloud, thermodynamic, and dynamic variability within the subtropical marine boundary layer, Atmos. Chem. Phys., 17, 9451-9468, https://doi.org/10.5194/acp-17-9451-2017, 2017.

Kärcher, B.: Cirrus clouds and their response to anthropogenic activities, Curr. Clim. Change Rep., 3, 45–57, doi:10.1007/s40641-017-0060-3, 2017.

Krämer, M., Rolf, C., Luebke, A., and Coauthors: A microphysics guide to cirrus clouds – Part 1: Cirrus types, Atmos. Chem. Phys., 16, 3463–3483, 2016.

Keckhut, P., Borchi, F., Bekki, S., Hauchecorne, A., and Silaouina, M.: Cirrus classification at midlatitude from systematic lidar observations, J. Appl. Meteor. Climat., 45, 249–258, 2006.

Lawson, R. P., Jensen, E., Mitchell, D. L., Baker, B., Mo, Q., and Pilson, B.: Microphysical and radiative properties of tropical clouds investigated in TC4 and NAMMA, J. Geophys. Res., 115, D00J08, doi:10.1029/2009JD013017, 2010.

Leroy, D., Fontaine, E., Schwarzenboeck, A., and Coauthors: Ice crystal sizes in High Ice Water Content clouds. Part II: Statistics of mass diameter percentiles in tropical convection observed in the HAIC/HIWC project, J. Atmos. Ocean. Tech., 34, 117–136, 2017.

Lindzen, R. S., Chou, M.-D., and Hou, A. U.: Does the Earth have an adaptive infrared iris? Bull. Am. Meteorol. Soc. 82, 417–432, 2001.

Liu, X., Penner, J. E., Ghan, S. J., and Wang, M.: Inclusion of ice microphysics in the NCAR Community Atmospheric Model Version 3 (CAM3), J. Climate, 20, 4526–4547, 2007.

Luo, Z., Liu, G. Y., and Stephens, G. L: CloudSat adding new insight into tropical penetrating convection, Geophys. Res. Lett., 35, L19819, doi:10.1029/2008GL035330, 2008.

Mace, G. G., Zhang, Q., Vaughan, M., Marchand, R., Stephens, G., Trepte, C., and Winker, D.: A description of hydrometeor layer occurrence statistics derived from the first year of merged Cloudsat and CALIPSO data, J. Geophys. Res., 114, D00A26, doi:10.1029/2007JD009755, 2009.

Manaster, A., O'Dell, C., Elsaesser, G.: Evaluation of Cloud Liquid Water Path Trends Using a Multidecadal Record of Passive Microwave Observations, J. Climate, 30, 5871–5884, DOI: 10.1175/JCLI-D-16-0399.1, 2017.

Manning, E. M., and Aumann, H. H.: Hyperspectral sounder performance for cold scenes, Proc. SPIE 10402, Earth Observing Systems XXII, 1040225, http://dx.doi.org/10.1117/12.2273398, 2017.

Marvel, K., Zelinka, M., Klein, S. A., Bonfils, C., Caldwell, P., Doutriaux, C., Santer, B. D., and Taylor, K. E.: External influences on modeled and observed cloud trends, Journal of Climate, 28, 4820–4840, 2015.

Mauritsen, T., and Stevens, B.: Missing iris effect as a possible cause of muted hydrological change and high climate sensitivity in models, Nat. Geosci., doi:10.1038/ngeo2414, 2015.

McFarquhar, G. M., and Heymsfield, A. J.: The definition and significance of an effective radius for ice clouds. J. Atmos. Sci., 55, 2039–2052, doi:10.1175/1520-0469(1998)055<2039:TDASOA>2.0.CO;2, 1998.

Minnis, P., Sun-Mack, S., Young, D. F., and Coauthors: CERES edition-2 cloud property retrievals using TRMM VIRS and Terra and Aqua MODIS data, Part I: Algorithms. IEEE Trans. Geosci. Remote Sens., 49, 4374–4400, 2011.

Mitchell, D. L., Rasch, P., Ivanova, D., McFarquhar, G., and Nousiainen, T.: Impact of small ice crystal assumptions on ice sedimentation rates in cirrus clouds and GCM simulations, Geophys. Res. Lett., 35, L09806, doi:10.1029/2008GL033552, 2008.

Morrison, H., and Grabowski, W. W.: Cloud-system resolving model simulations of aerosol indirect effects on tropical deep convection and its thermodynamic environment, Atmos. Chem. Phys., 11, 10503–10523, 2011.

Nasiri, S. L., Dang, V. T., Kahn, B. H., and Coauthors: Comparing MODIS and AIRS infrared-based cloud retrievals, J. Appl. Meteorol. Climatol., 50, 1057–1072, doi:10.1175/2010JAMC2603.1, 2011.

Norris, J. R., Allen, R. J., Evan, A. T., Zelinka, M. D., O'Dell, C. W., and Klein, S. A.: Evidence for climate change in the satellite cloud record, Nature, 536, 72–75, https://doi.org/10.1038/nature18273, 2016.

Pagano, T. S., Broberg, S., Aumann, H. H., Elliott, D., Manning, E., and Strow, L.: Performance status of the Atmospheric Infrared Sounder ten years after launch, Proc. SPIE 8527, Multispectral, Hyperspectral, and Ultraspectral Remote Sensing Technology, Techniques and Applications IV, 852703, http://dx.doi.org/10.1117/12.977309, 2012.

Phillips, V. T. J., Donner, L. J., and Garner, S. T.: Nucleation processes in deep convection simulated by a cloud-system-resolving model with double-moment bulk microphysics, J. Atmos. Sci., 64, 738–761, 2007.

Platnick, S., Meyer, K. G., King, M. D., and Coauthors: The MODIS cloud optical and microphysical products: Collection 6 updates and examples from Terra and Aqua. IEEE Trans. Geosci. Remote Sens., 55, 502–525, doi:10.1109/TGRS.2016.2610522, 2017.

Posselt, D., L'Ecuyer, T. S., and Stephens, G. L.: Exploring the error characteristics of thin ice cloud property retrievals using a Markov chain Monte Carlo algorithm, J. Geophys. Res., 113, D24206, doi:10.1029/2008JD010832, 2008.

Protopapadaki, S. E., Stubenrauch, C. J., and Feofilov, A. G.: Upper tropospheric cloud systems derived from IR sounders: properties of cirrus anvils in the tropics, Atmos. Chem. Phys., 17, 3845-3859, https://doi.org/10.5194/acp-17-3845-2017, 2017.

Protat, A., Delanoë, J., May, P. T., Haynes, J., Jakob, C., O'Connor, E., Pope, M., and Wheeler, M. C.: The variability of tropical ice cloud properties as a function of the large-scale context from ground-based radar-lidar observations over Darwin, Australia, Atmos. Chem. Phys., 11, 8363–8384, 2011.

Rosenfeld, D., Lohmann, U., Raga, G. B., and Coauthors: Flood or drought: How do aerosols affect precipitation? Science, 321, 1309–1313, doi:10.1126/science.1160606, 2008.

Rysman, J.-F., Claud, C., and Delanoë, J: Monitoring deep convection and convective overshooting from 60º S to 60º N using MHS: A CloudSat/CALIPSO-based assessment, IEEE Geosci. Remote Sens. Lett., 14, 159–163, 2017.

Sanderson, B. M., Piani, C., Ingram, W. J., Stone, D. A., and Allen, M. R.: Towards constraining climate sensitivity by linear analysis of feedback patterns in thousands of perturbed-physics GCM simulations, Clim. Dyn., 30, 175–190, 2008.

Santer, B. D., Wigley, T. M. L., Boyle, J. S., Gaffen, D. J., Hnilo, J. J., Nychka, D., Parker, D. E., and Taylor, K. E.: Statistical significance of trends and trend differences in layer-average atmospheric temperature time series, J. Geophys. Res., 105, 7337–7356, 2000.

Satoh, M., and Matsuda, Y.: Statistics on high-cloud areas and their sensitivities to cloud microphysics using single-cloud experiments, J. Atmos. Sci., 66, 2659–2677, 2009.

Sherwood, S. C.: Aerosols and ice particle size in tropical cumulonimbus, J. Climate, 15, 1051–1063, 2002.

Stanford, M. W., Varble, A., Zipser, E., Strapp, J. W., Leroy, D., Schwarzenboeck, A., Potts, R., and Protat, A.: A ubiquitous ice size bias in simulations of tropical deep convection, Atmos. Chem. Phys., 17, 9599–9621, 2017.

Stephens, G. L.: The influence of radiative transfer on the mass and heat budgets of ice crystals falling in the atmosphere, J. Atmos. Sci., 40, 1729–1739, 1983.

Stubenrauch, C., Rossow, W. B., Kinne, S., and Coauthors: Assessment of global cloud datasets from satellites: Project and database initiated by the GEWEX Radiation Panel. Bull. Amer. Meteor. Soc., 94, 1031–1049, doi:https://doi.org/10.1175/BAMS-D-12-00117.1, 2013.

Su, H., Jiang, J. H., Neelin, J. D., and Coauthors: Tightening of tropical ascent and high clouds key to precipitation change in a warmer climate, Nat. Comm., doi:10.1038/ncomms15771, 2017.

Takahashi, H., and Luo, Z.: Where is the level of neutral buoyancy for deep convection?. Geophys. Res. Lett., 39, DOI:10.1029/2012GL052638, 2012.

Takahashi, H. and Luo, Z. J.: Characterizing tropical overshooting deep convection from joint analysis of CloudSat and geostationary satellite observations. J. Geophys. Res. Atmos., 119, 112–121, 2014.

Takahashi, H., Luo, Z. J., and Stephens, G. L.: Level of neutral buoyancy, deep convective outflow, and convective core: New perspectives based on 5 years of CloudSat data, J. Geophys. Res. Atmos, 122, 2958–2969, DOI:10.1002/2016JD025969, 2017.

van Diedenhoven, B., Fridlind, A. M., Cairns, B., and Ackerman, A. S.: Variation of ice crystal size, shape, and asymmetry parameter in tops of tropical deep convective clouds, J. Geophys. Res. Atmos., 119, 11809–11825, 2014.

van Diedenhoven, B., Fridlind, A. M. , Cairns, B., Ackerman, A. S., and Yorks, J. E.: Vertical variation of ice particle size in convective cloud tops, Geophys. Res. Lett., 43, 4586–4593, 2016.

Van Weverberg, K., Vogelmann, A. M., Lin, W., Luke, E. P., Cialella, A., Minnis, P., Khaiyer, M., Boer, E. R., and Jensen, M. P.: The role of cloud microphysics parameterization in the simulation of mesoscale convective system clouds and precipitation in the tropical western Pacific, J. Atmos. Sci., 70, 1104–1128, 2013.

Wang, C., Platnick, S., Zhang, Z., Meyer, K., and Yang, P: Retrieval of ice cloud properties using an optimal estimation algorithm and MODIS infrared observations: 1. Forward model, error analysis, and information content, J. Geophys. Res. Atmos., 121, doi:10.1002/2015JD024526, 2016.

Wylie, D., Jackson, D. L., Menzel, W. P., and Bates, J. J.: Trends in global cloud cover in two decades of HIRS observations, J. Climate, 18, 3021–3031, 2005.

Yuan, T., and Li, Z.: General macro- and microphysical properties of deep convective clouds as observed by MODIS, J. Climate, 23, 3457–3473, 2010.

Yue, Q., Kahn, B. H., Fetzer, E. J., Wong, S., Frey, R., and Meyer, K. G.: On the response of MODIS cloud coverage to global mean surface air temperature, J. Geophys. Res.-Atmos., 122, 966–979, https://doi.org/10.1002/2016JD025174, 2017a.

Yue, Q., Lambrigtsen, B., Behrangi, A., and Coauthors: AIRS V6 Test Report Supplement: Performance of AIRS+AMSU vs. AIRS-only retrievals: Analysis of the impact of the loss of AMSU-A2, 104 pp., 2017b.

Zelinka, M. D., Klein, S. A., Taylor, K. E., and Coauthors: Contributions of different cloud types to feedbacks and rapid adjustments in CMIP5. J. Climate, 26, 5007–5027, doi:10.1175/JCLI-D-12-00555.1, 2013.

Zhang, Z., Platnick, S., Yang, P., Heidinger, A. K., and Comstock, J. M.: Effects of ice particle size vertical inhomogeneity on the passive remote sensing of ice clouds, J. Geophys. Res., 115, D17203, doi:10.1029/2010JD013835, 2010.

	Mean Difference (Perturbed – Baseline IR/MW)		Median Absolute Deviation (Perturbed – Baseline IR/MW)	
	+50 mK	+50 mK before CC	+50 mK	+50 mK before CC
r_{ei} (μm)	-0.105	-0.131	0.786	1.168
r_{ei} AK	-9.15×10^{-5}	$+2.05\times10^{-6}$	0.00278	0.00247
τ_i	+0.00534	+0.0101	0.0812	0.149
τ_i AK	-0.00117	-2.35×10^{-4}	0.0108	0.0053
T_{ice} (K)	+0.261	+0.235	1.179	2.187
T_{ice} AK	$+4.73\times10^{-4}$	+0.00113	0.00852	0.00999
χ^2	-0.0176	-0.0315	0.54	0.648

Table 1. Shown are the two radiance perturbation tests after cloud clearing (+50 mK) and before cloud clearing (+50 mK before CC); see text for description), with reported mean difference and median absolute deviations of cloud properties, AKs, and χ^2 for 54°S-54°N over ocean for 6 September 2002.

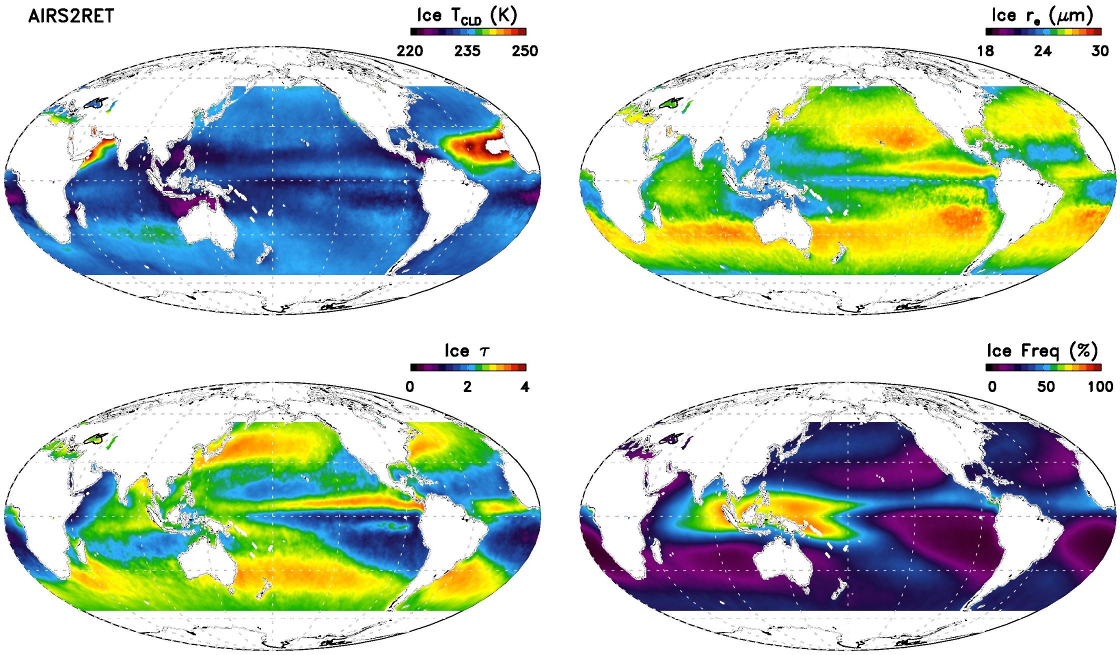

Figure 1: Shown are the global 14-year averages (1 September 2002 –31 August 2016) of T_{ci}, r_{ei}, τ_i, and ice cloud frequency, for the AIRS IR only retrieval (AIRS2RET) between 54°S-54°N over the oceans.

Atmos. Chem. Phys. Discuss., https://doi.org/10.5194/acp-2017-1216
Manuscript under review for journal Atmos. Chem. Phys.
Discussion started: 31 January 2018

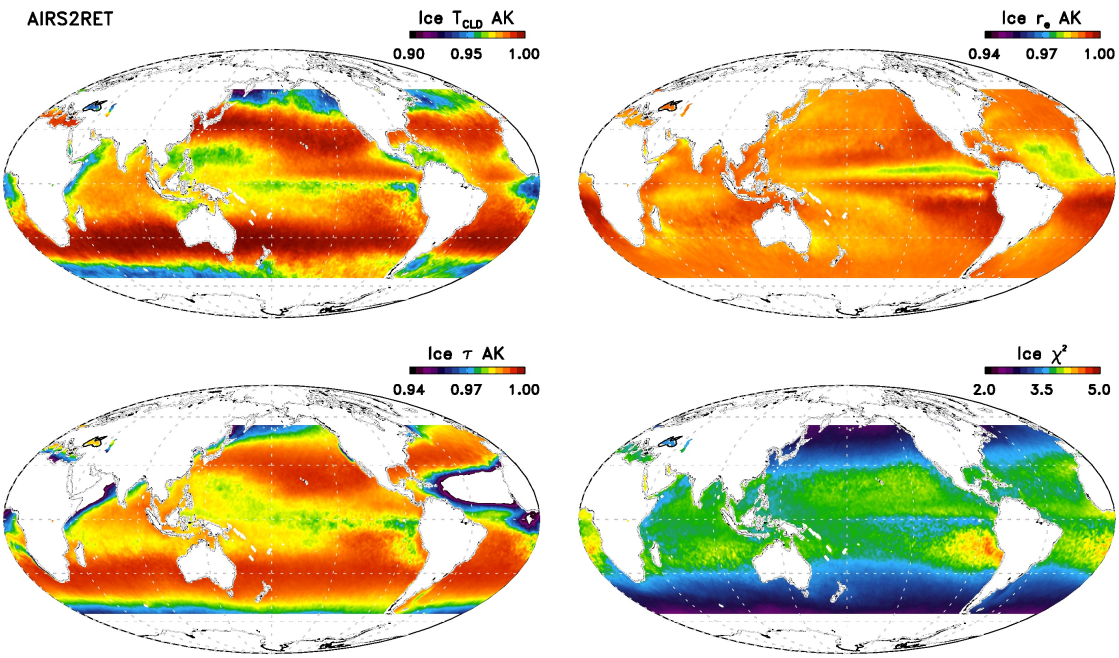

Figure 2: Same as Fig. 1 except are the global 14-year averages of T_{ci}, r_{ei}, and τ_i averaging kernels (AKs) and χ^2 fitting parameter.

Atmos. Chem. Phys. Discuss., https://doi.org/10.5194/acp-2017-1216
Manuscript under review for journal Atmos. Chem. Phys.
Discussion started: 31 January 2018

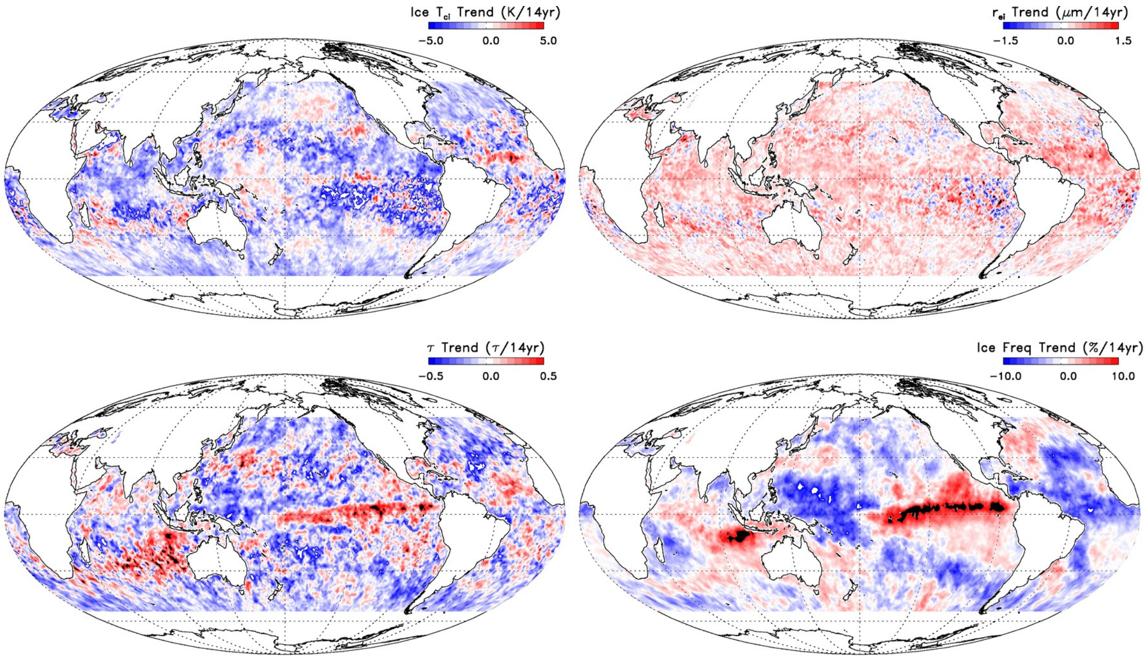

Figure 3: Shown are the global 14-year trends for the fields in Fig. 1.

Atmos. Chem. Phys. Discuss., https://doi.org/10.5194/acp-2017-1216
Manuscript under review for journal Atmos. Chem. Phys.
Discussion started: 31 January 2018

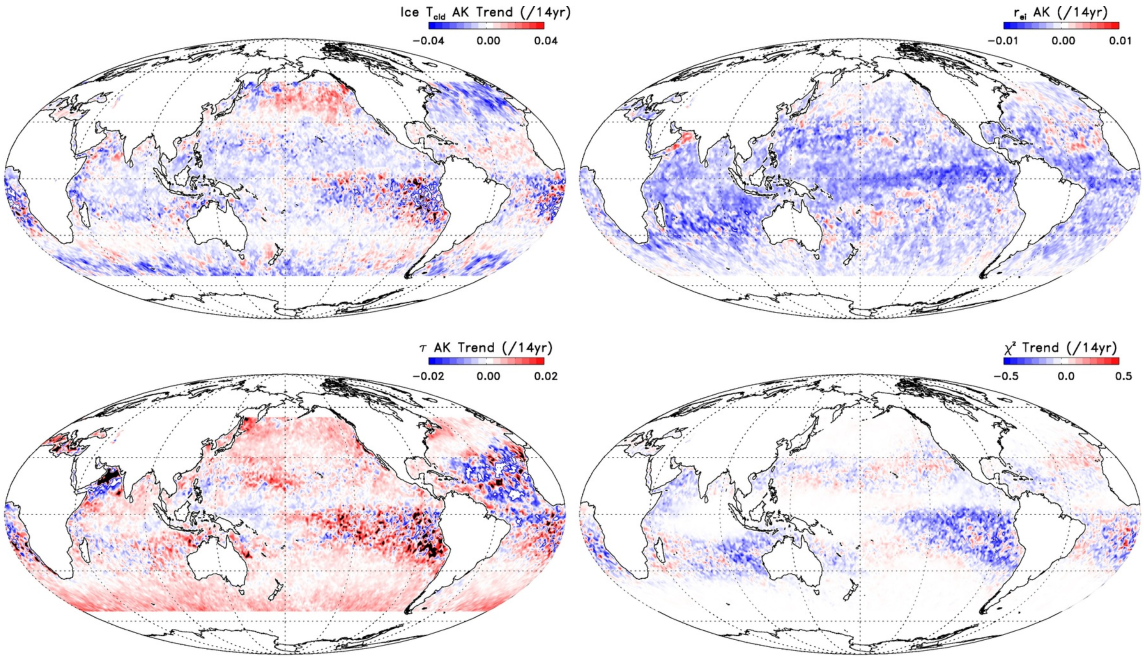

Figure 4: Shown are the global 14-year trends for the fields in Fig. 2.

Atmos. Chem. Phys. Discuss., https://doi.org/10.5194/acp-2017-1216
Manuscript under review for journal Atmos. Chem. Phys.
Discussion started: 31 January 2018

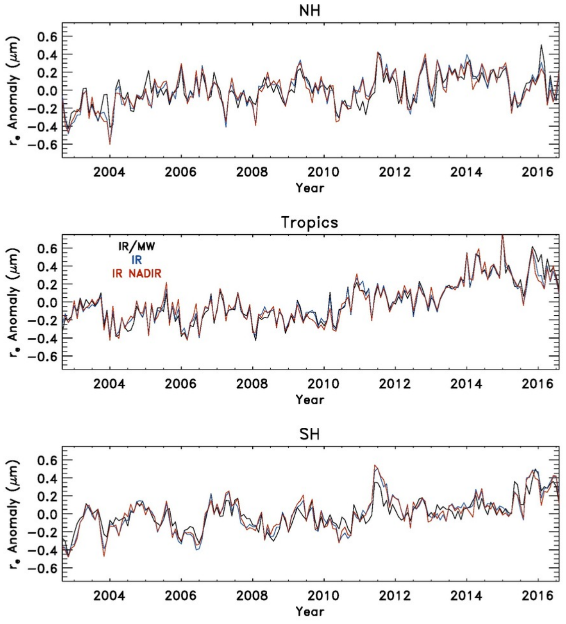

Figure 5: Monthly anomaly time series for r_{ei} for the IR/MW, IR only, and IR nadir retrievals organized into three latitude bands: SH extratropics (54°S-18°S), tropics 18°S-18°N, and NH extratropics (18°N-54°N).

5

Atmos. Chem. Phys. Discuss., https://doi.org/10.5194/acp-2017-1216
Manuscript under review for journal Atmos. Chem. Phys.
Discussion started: 31 January 2018

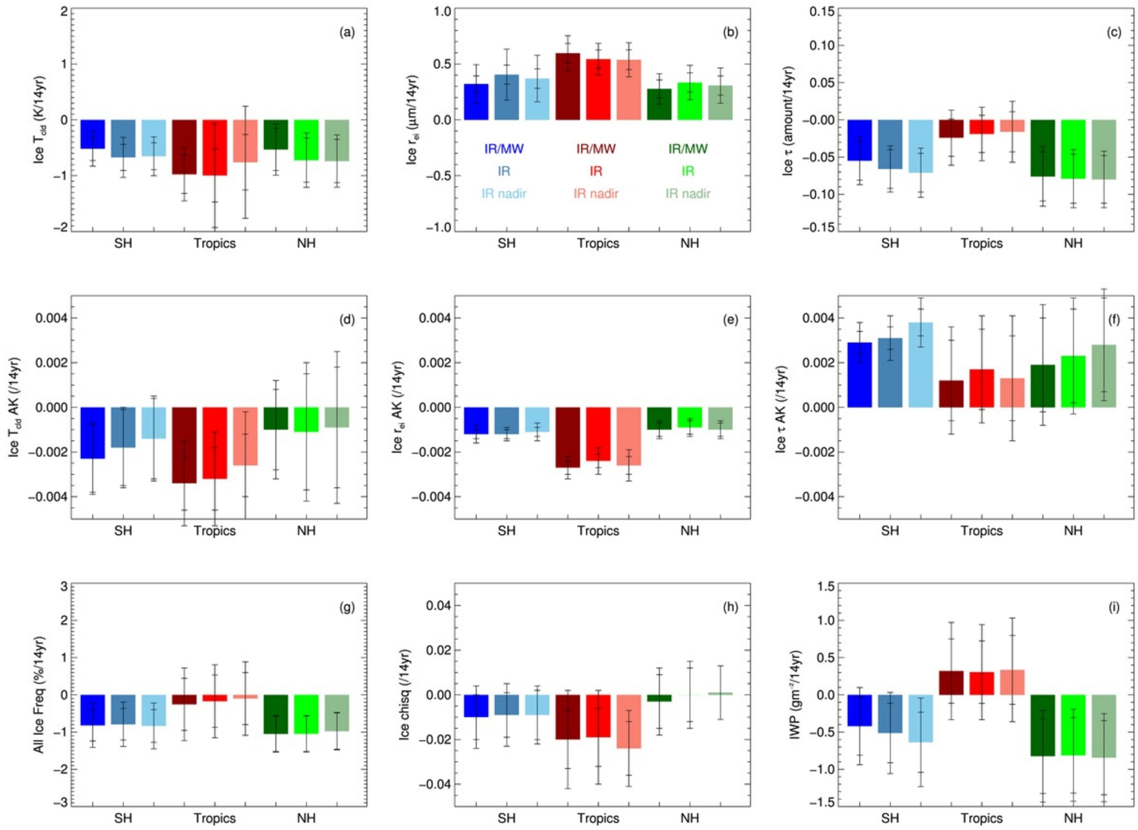

Figure 6: Shown are the 14-year trends for the tropics, SH and NH extratropics, and IR/MW, IR only, and IR nadir retrievals. (a) T_{ci}, (b) r_{ei}, (c) τ_i, (d) T_{ci} AK, (e) r_{ei} AK, (f) τ_i AK, (g) ice cloud frequency, (h) χ^2, (i) IWP. The confidence for 95% statistical significance is shown as black lines with narrow tick marks and the confidence for 95% statistical significance with a lag-1 autocorrelation correction as wider tick marks (see Santer et al., 2000).

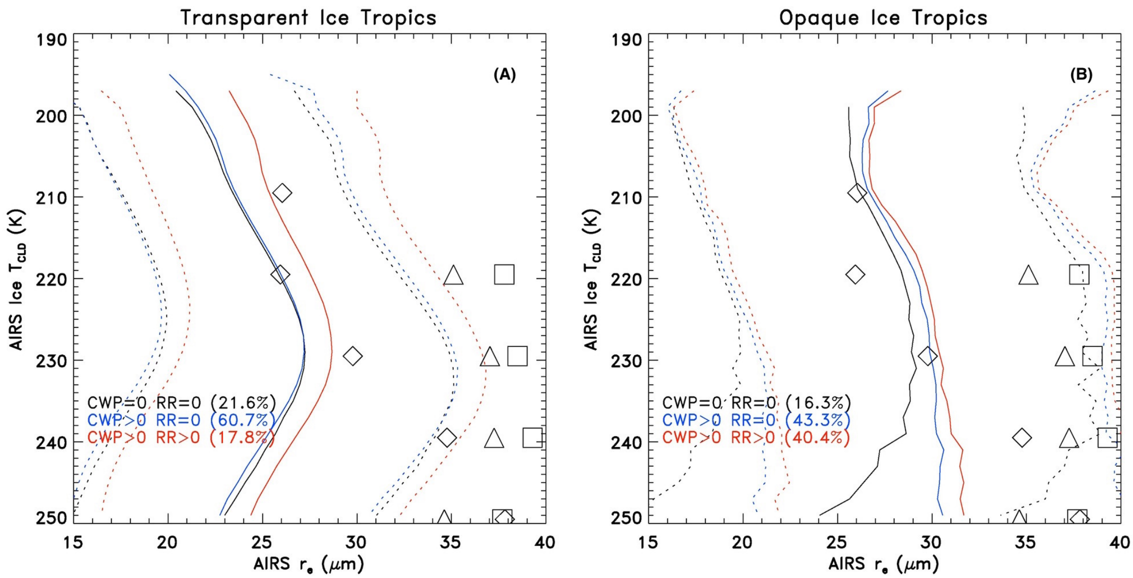

Figure 7. Shown are the mean (solid) and ±1σ values of AIRS IR only r_{ei} versus T_{ci} for (a) transparent and (b) opaque ice clouds over the tropical oceans during the months of July and August within the 14-year time period of investigation. Following the approach of Protopapadaki et al. (2017), transparent and opaque clouds are delineated using a threshold effective cloud fraction value of ECF ≤ 0.98 for transparent and ECF > 0.98 for opaque, The AMSR-E/AMSR-2 estimates of CWP and RR are used to divide categories into clear (CWP=0) and no rain (RR=0) according to the passive microwave; cloudy (CWP>0) and no rain (RR=0); and cloudy (CWP>0) and rain (RR>0). The results in both panels have all AIRS ice clouds filtered within 6 K of the cold point tropopause; otherwise a much larger and potentially unphysical increase in r_{ei} would be observed in the figures. The symbols are average r_{ei} from in situ field campaign data for the CRYSTAL-FACE (diamonds), TC4 (triangles), and NAMMA (squares) campaigns, please see text and Heymsfield et al. (2014) for more details.

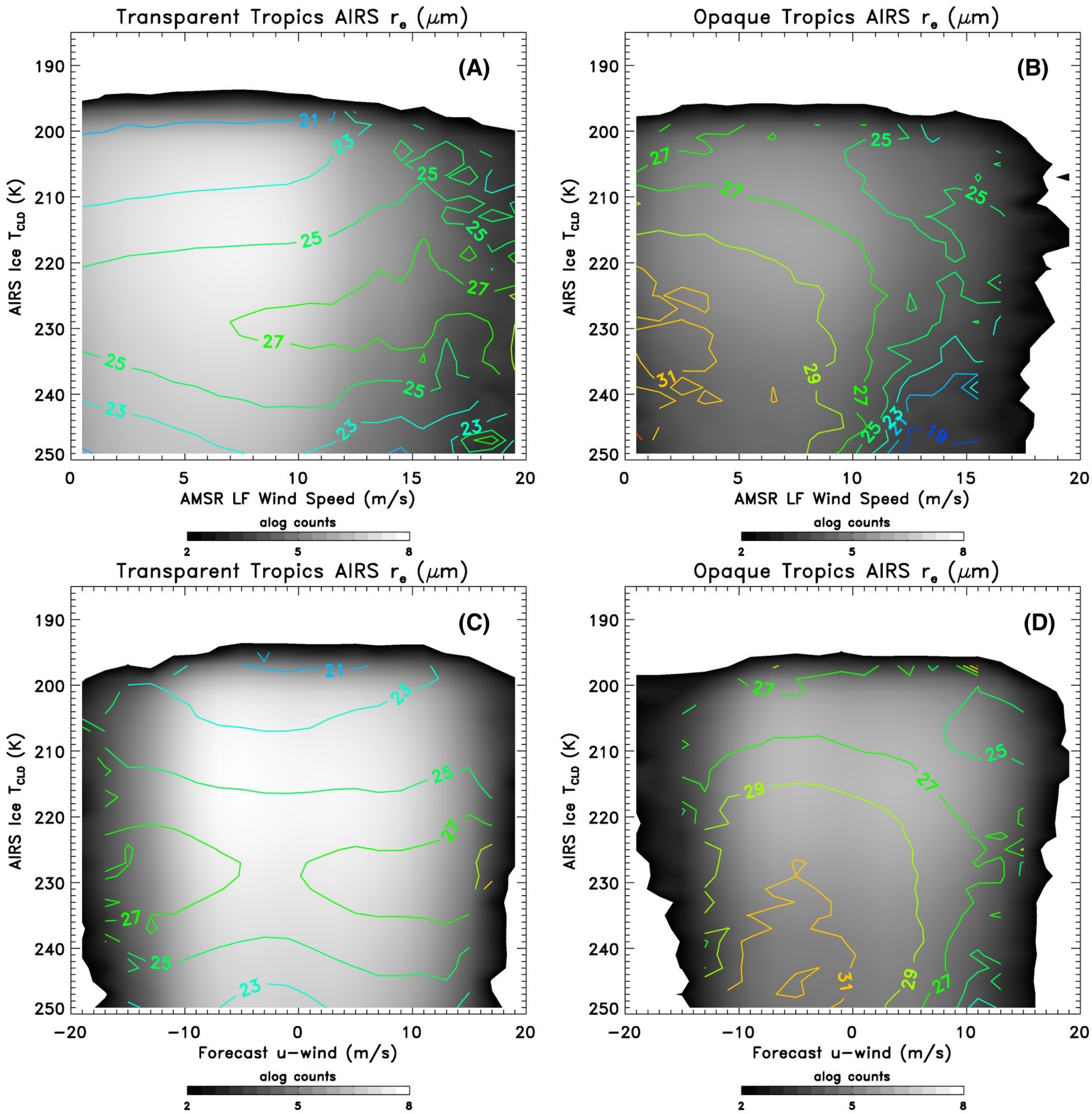

Figure 8. Shown are AMSR-E/AMSR-2 low frequency (LF) wind speeds (m s^{-1}) versus T_{ci} histograms, with the log counts shown as a gray scale, the AIRS IR only r_{ei} (µm) overlaid as colored contours, and transparent (a) and opaque (b) clouds shown separately. In the lower row, it is the same as the upper row except for NWP model u-component wind speeds for (c) transparent and (d) opaque clouds.

Atmos. Chem. Phys. Discuss., https://doi.org/10.5194/acp-2017-1216
Manuscript under review for journal Atmos. Chem. Phys.
Discussion started: 31 January 2018

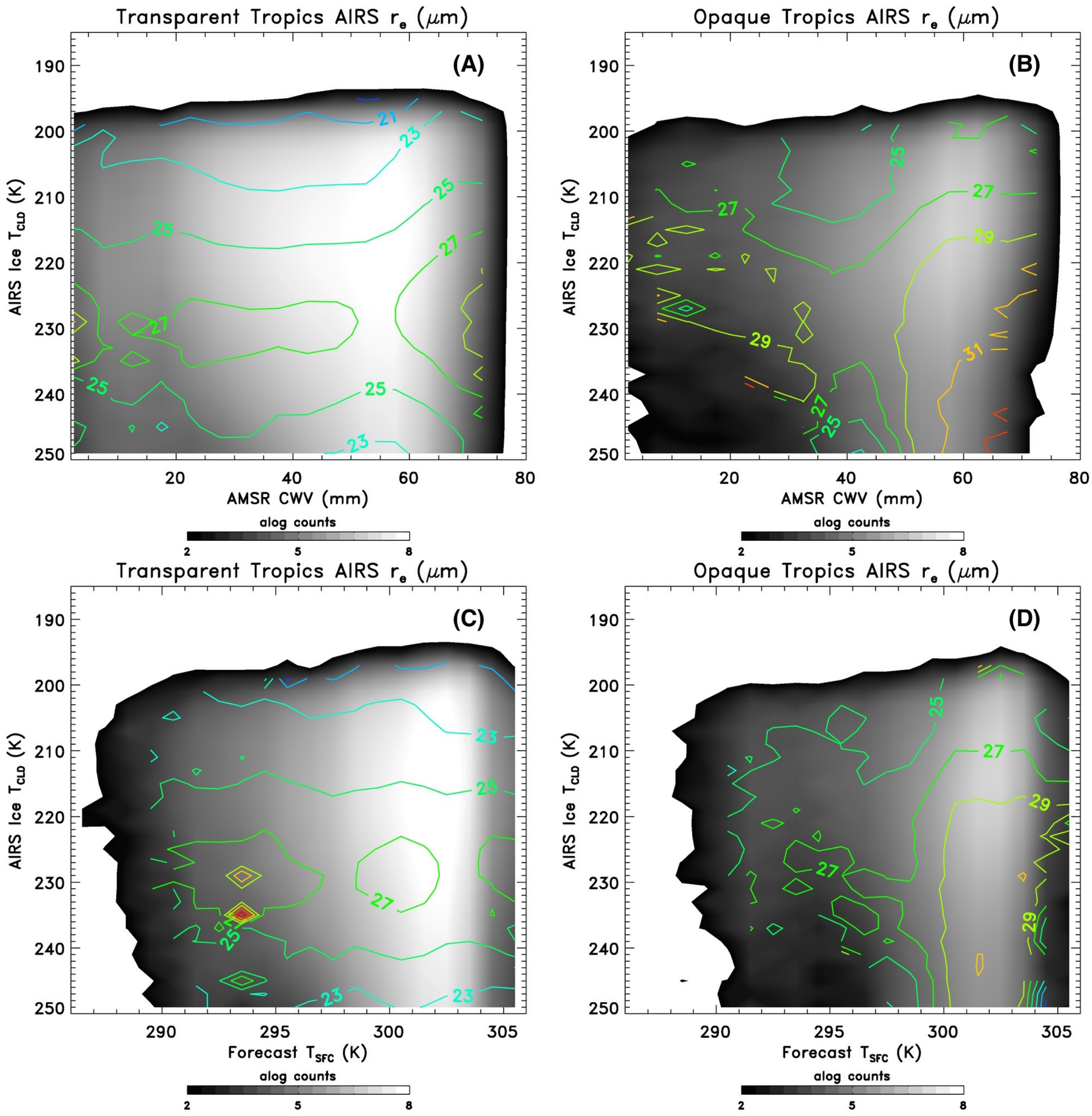

Figure 9. Shown are AMSR-E/AMSR-2 total CWV (mm) versus T_{ci} histograms, with the log counts shown as a gray scale, the AIRS IR only r_{ei} (µm) overlaid as colored contours, for (a) transparent and (b) opaque clouds separately. In the lower row, it is the same as the upper row except for T_{sfc} (K) for (c) transparent and (d) opaque clouds separately.

5

Atmos. Chem. Phys. Discuss., https://doi.org/10.5194/acp-2017-1216
Manuscript under review for journal Atmos. Chem. Phys.
Discussion started: 31 January 2018

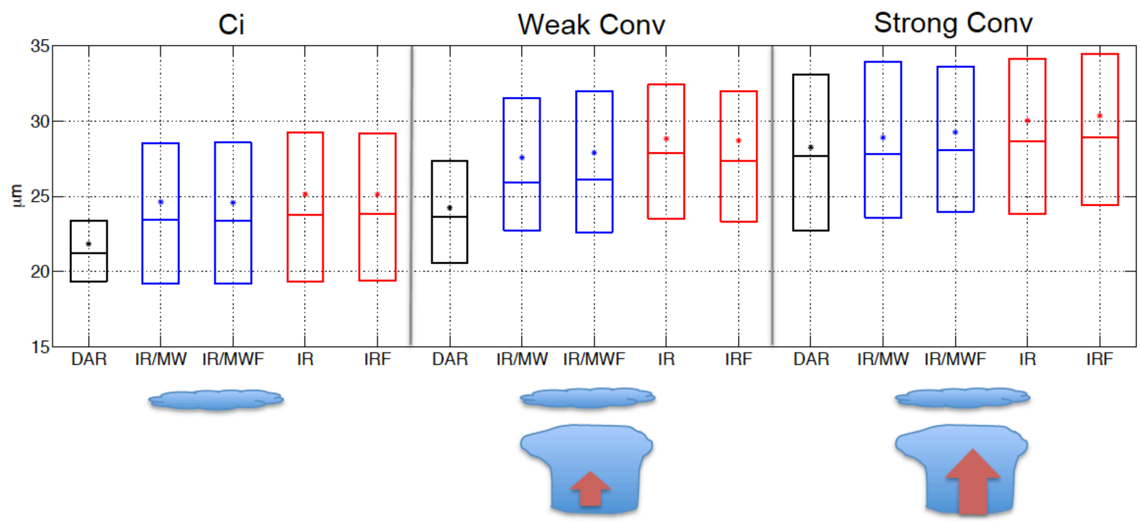

Figure 10. DARDAR (black), IR/MW (blue) and IR only (red) retrievals of r_{ei} in single-layered cirrus (left), cirrus on top of weak convection (center), and cirrus on top of strong convection (right); see Section 2.3 for a description of the definition of convective intensity. The AIRS retrievals are also shown for a filtered version that removes retrievals within 6 K of the tropopause. The central line is the median, the asterisk is the mean, and the bottom and top edges of the boxes are the 25th and 75th percentiles.

Atmos. Chem. Phys. Discuss., https://doi.org/10.5194/acp-2017-1216
Manuscript under review for journal Atmos. Chem. Phys.
Discussion started: 31 January 2018

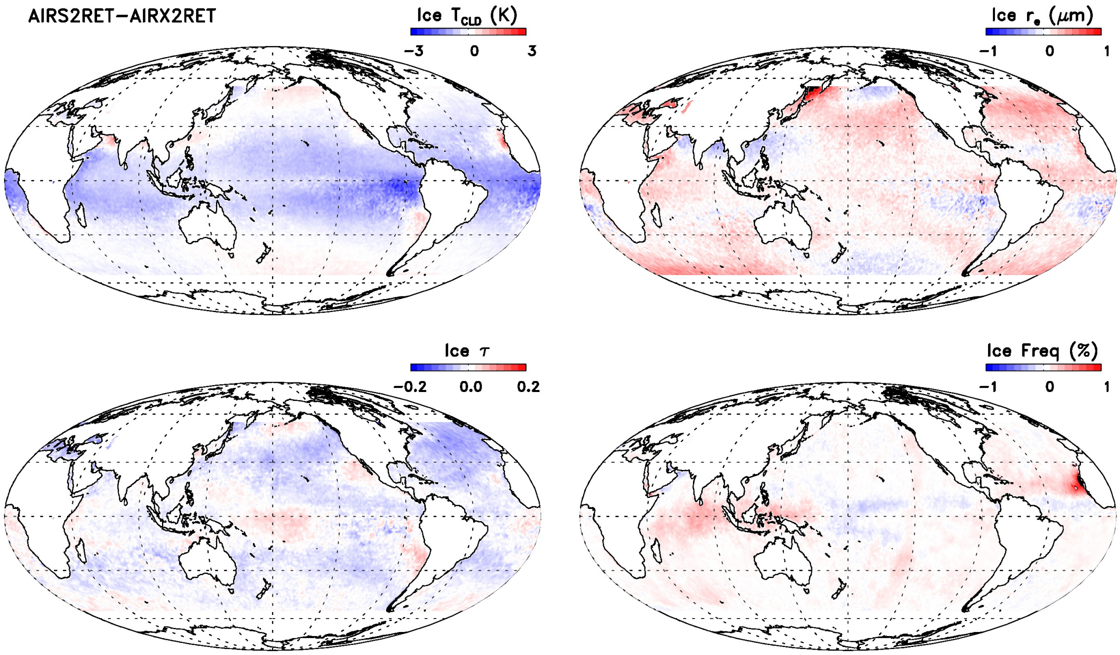

Figure A1: Shown are the differences in IR only (AIRS2RET) minus IR/MW (AIRX2RET) for the same time period as described in Fig. 1 for T_{ci}, r_{ei}, τ_i, and ice cloud frequency.

Atmos. Chem. Phys. Discuss., https://doi.org/10.5194/acp-2017-1216
Manuscript under review for journal Atmos. Chem. Phys.
Discussion started: 31 January 2018

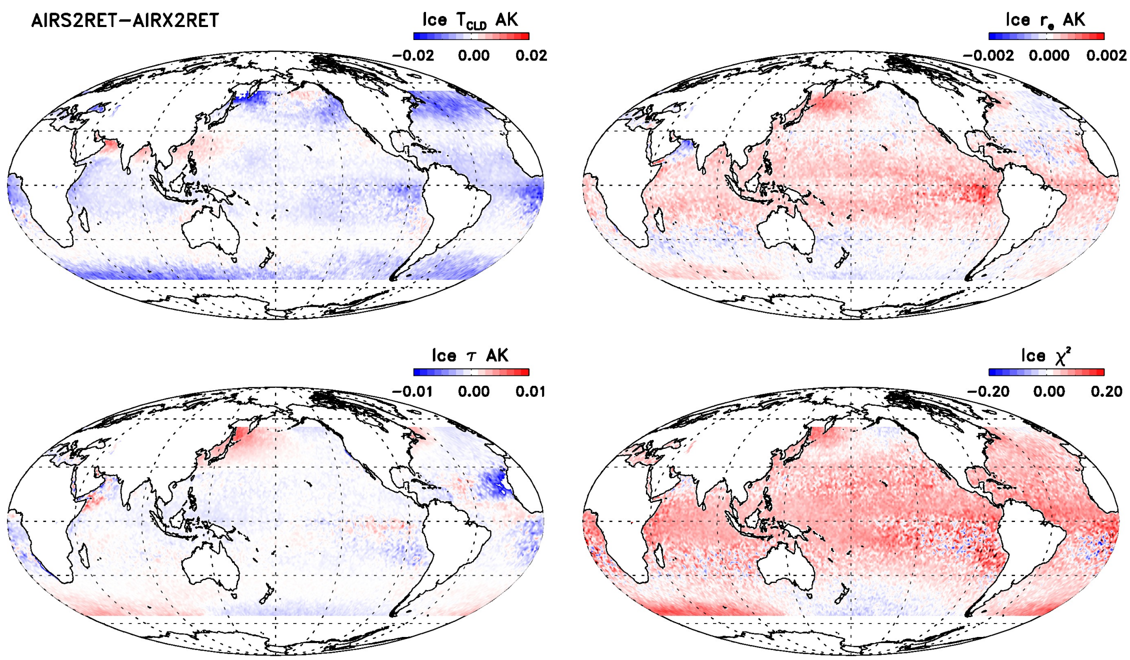

Figure A2: Same as Fig. A1, except for the T_{ci}, r_{ei}, and τ_i AKs, and the χ^2 fitting parameter.